Time-constrained multiphase brittle tectonic evolution of the onshore mid-Norwegian passive margin

Time-constrained multiphase brittle tectonic evolution of the onshore mid-Norwegian Passive Margin

Giulia Tartaglia*[1], Alberto Ceccato[1], Thomas Scheiber[2], Roelant van der Lelij[3], Jasmin Schönenberger[3] and Giulio Viola*[1]

[1] *Alma Mater Studiorum of Bologna, Department of Biological, Geological and Environmental Sciences, Bologna, Italy*

[2] *Western Norway University of Applied Sciences, Department of Environmental Sciences, Sogndal, Norway*

[3] *Geological Survey of Norway, Trondheim, Norway*

**Corresponding authors: giulia.tartaglia4@unibo.it; giulio.viola3@unibo.it*

ABSTRACT

The mid-Norwegian Passive Margin (MNPM) is a multiphase rifted margin developed since the Devonian. Its geometry is affected by the long-lived activity of the Møre-Trøndelag Fault Complex (MTFC), an ENE-WSW oriented regional tectonic structure. We propose a time-constrained evolutionary scheme for the MNPM brittle history. By means of remote sensing lineament detection, field work, microstructural analysis, paleostress inversion, mineralogical characterization and K-Ar dating of fault rocks, six tectonic events have been identified: i) Paleozoic NE-SW compression forming WNW-ESE striking thrust faults; ii) Paleozoic NW-SE transpression forming conjugate strike-slip faults; iii) Carboniferous proto-rifting forming NW-

SE and NE-SW striking faults; iv) Late Triassic-Jurassic (c. 202 and 177 Ma) E-W extension forming ca. N-S striking epidote and quartz-coated normal faults and widespread alteration; v) renewed rifting in the Early Cretaceous (c. 122 Ma) with a NW-SE extension direction; vi) Late Cretaceous extensional pulses (c. 71, 80, 86, 91 Ma ago) reactivating pre-existing faults and crystallizing prehnite and zeolite. Our multidisciplinary and multiscalar study sheds light onto the structural evolution of the MNPM and confirms the active role of the MTFC during the rifting stages. Our sixty-two new radiometric K-Ar ages define discrete episodes of faulting along the MNPM. The proposed workflow may assist the interpretation of the structural framework of the MNPM offshore domain and also help to better understand fault patterns of fractured passive margins elsewhere.

1. INTRODUCTION AND AIMS OF THE STUDY

Passive margins are major morpho-tectonic features of the Earth resulting from extension within continents and the eventual tearing of continental lithosphere to form plate margins and oceanic basins. In addition to the first-order general features common to all margins around the globe, some passive margins may also exhibit remarkable local geological complexities and peculiarities that reflect i) their generally complex polyphase faulting history, with strain and deformation variably distributed in space and through time (Reston, 2005; Duffy et al., 2015; Will and Frimmel, 2018; Phillips et al., 2019; Zastrozhnov et al., 2020); ii) the effects of variably oriented and diachronic subsidiary rifting pulses that pre- and postdate the main rifting phase (Doré et al., 1999; Ren et al., 2003); iii) the effects of the spatial orientation of old, inherited structures, which generally represent zones of mechanical weakness within the crust and tend to preferentially localize rifting (Phillips et al., 2019; Schiffer et al., 2019).

The mid-Norwegian Passive Margin (MNPM) is an archetypal multiphase rifted margin that underwent a progressive evolution from the late orogenic collapse of the Caledonian belt in the Early Devonian down to the Late Eocene (Faleide et al., 2008; Theissen-Krah et al., 2017; Péron-Pinvidic and Osmundsen, 2020). It trends c. NE-SW and its southwestern termination intersects the N-S North Sea margin. Its distinctive oblique geometry compared to the North Sea margin is mainly due to the inherited structural grain of the Møre-Trøndelag Fault Complex (MTFC), an ENE-WSW trending crustal-scale shear zone in mid-Norway (e.g., Séranne, 1992; Redfield et al., 2004; Osmundsen et al., 2006; Schiffer et al., 2019; Gernigon et al., 2020; Péron-Pinvidic et al., 2020). While the details of the shear zone's complex faulting history are still being studied and discussed, it is widely accepted that the MTFC has been active at least from the Late Silurian-Early Devonian to the present-day (Séranne, 1992; Braathen et al., 1999, 2002; Osmundsen et al., 2005; Redfield et al., 2005; Sherlock et al., 2004; Nasuti et al., 2011).

The discovery of significant unconventional hydrocarbon reserves within exhumed offshore fractured and weathered crystalline basement blocks of the MNPM (e.g., Petford and McCaffrey, 2003; Riber et al., 2015, 2017; Trice et al., 2019) has caused a surge of interest in the geometry, petrophysical properties and development of intra-basement fracture networks and weathering in the context of passive margin evolution (e.g., Fossen, 2010; Breivik et al., 2011; Riber et al., 2015; Fredin et al., 2017; Scheiber and Viola, 2018; Trice et al., 2019; Fazlikhani et al., 2020; Ceccato et al., 2021a, b). The MNPM is indeed characterized by a dense network of lineaments that are the expression of brittle fault and fracture zones cumulated during the margin's long and multiphase brittle evolution (Gabrielsen et al., 2002). They occur within both on- and offshore basement units (Fredin et al., 2017; Trice et al., 2019). The structural brittle template of the offshore domain has been mainly studied by seismic imaging and drilling. Currently available

65 geophysical techniques permit to only detect fracture and fault zones characterized by minimum
66 detectable throws >5-20 m, the so-called seismic-resolution scale features (Tanner et al., 2019).
67 On the other hand, onshore structural analysis permits to also study smaller brittle features at a
68 sub-seismic resolution scale (Braathen et al., 2004; Redfield and Osmundsen, 2009; Ksienzyk et
69 al., 2016; Scheiber and Viola, 2018; Scheiber et al., 2019; Ceccato et al., 2021a), which are key
70 to the definition of the structural permeability of basement blocks. A detailed study of the brittle
71 fault network exposed on onshore domains and of the related brittle deformation history can,
72 therefore, assist the reconstruction and interpretation of the regional geological framework and
73 evolution of the offshore domain, leading to high-resolution integrated models for the structural
74 evolution recorded by passive margins (e.g., Redfield and Osmundsen, 2009; Ksienzyk et al.,
75 2016; Gabrielsen et al., 2018; Scheiber and Viola, 2018) and better exploration predictive tools.

76 While decades of petroleum exploration have unveiled the fine details of the regional structure of
77 the offshore domain of the MNPM (e.g., Theissen-Krah et al., 2017; Gernigon et al., 2020;
78 Zastrozhnov et al., 2020 and references therein), so far only a few studies have focused on its
79 onshore counterpart, with the notable exception of the MTFC (e.g., Gabrielsen et al., 1999;
80 Kendrick et al., 2004; Redfield et al., 2004; Osmundsen et al., 2006; Nasuti et al., 2011).
81 Furthermore, although the polyphase evolution of the MNPM is quite well known and
82 established, absolute age constraints on its brittle faulting events are still largely missing, thus
83 preventing detailed reconstructions and correlations along and across the margin.

84 The intricated network of brittle fractures and faults affecting the offshore MNPM and the lack
85 of well dated sedimentary markers makes retrieving an absolute time sequence for its
86 deformation history a challenging task. All these difficulties notwithstanding, some studies have
87 demonstrated that it is possible to unravel complex brittle histories by studying the details of

88 geometric, kinematic, and geochronological brittle deformation features (e.g., Wilson et al.,
89 2006; Viola et al., 2009; Saintot et al., 2011; Lacombe et al., 2013; Mattila and Viola, 2014;
90 Scheiber and Viola, 2018; Nordbäck et al., 2022). A significant contribution in this respect stems
91 from the possibility to radiometrically date fault rocks associated with key structural features of
92 the margins so as to add absolute time constraints to brittle structural reconstructions (van der
93 Pluijm et al., 2001; Zwingmann and Mancktelow, 2004; Davids et al., 2013; Torgersen et al.,
94 2015; Ksienzyk et al., 2016; Vrolijk et al., 2018; Tartaglia et al., 2020; Fossen et al., 2021).

95 Aiming at better constraining the evolution of the MNPM, we present the results of a combined
96 multidisciplinary and multiscalar structural-geochronological study focusing on the post-
97 Caledonian evolution of the onshore MNPM and, for the first time, propose a time-constrained
98 evolutionary scheme for its brittle history based on sixty-two new K-Ar ages obtained from some
99 of its representative onshore fault zones. Our conceptual and analytical approach is of general
100 validity and may be useful to unravel complex brittle histories of similar tectonic settings
101 elsewhere.

102 2. GEOLOGICAL SETTING

103 The MNPM forms a 350-500 km wide sector of rifted and hyperextended continental crust
104 facing the Norwegian-Greenland Sea (Northeastern Atlantic Ocean; Fig. 1). The studied offshore
105 part of the MNPM is composed of two large segments, which, from SW to NE, include the Møre
106 and the Vøring margins (Fig. 1). Discrete, NW-SE-trending tectonic structures, such as the Jan
107 Mayen Corridor, separate these segments (Faleide et al., 2008; Gernigon et al., 2020), each of
108 which contains an inner platform, the Møre, and Vøring Platforms, and a system of outer basins,
109 the Møre and the Vøring Basins (Fig. 1). The studied onshore portion of the MNPM between 61°

54’ N and 63° 55’ N is mainly located within the Western Gneiss Region (WGR), (Fig. 1), which is, generally composed of pervasively foliated Proterozoic gneisses locally hosting micaschist, amphibolite and eclogite lenses (Krabbendam and Dewey, 1998; Corfu et al., 2014). The formation of the MNPM results from a long extensional history that started with the collapse of the Scandinavian Caledonides in the Late Silurian-Devonian and continued by deformation localized during discrete tectonic pulses down to the breakup of Greenland from Scandinavia in the early Eocene (Doré et al., 1999; Stemmerik et al., 2000; Faleide et al., 2008; Gernigon et al., 2020). Based on sedimentary and structural observations onshore East Greenland, the initiation of rifting is constrained to the mid-Carboniferous, while it is poorly constrained in the MNPM (e.g., Stemmerik et al., 2000; Rotevatn et al., 2018). By this time, the WGR was exhumed to shallow (<10 km) crustal levels, as inferred from the Early-Middle Devonian (380-400 Ma) muscovite ^{40}Ar-^{39}Ar cooling ages from the area (Kendrick et al., 2004; Walsh et al., 2013).

The MNPM accommodated two main phases of rifting, in the Permo-Triassic and Late Jurassic-Cretaceous, respectively (Gernigon et al., 2020), with its early rifting history strongly controlled by the structural grain inherited from the Caledonian orogen (Doré et al., 1997; Schiffer et al., 2019). During the ENE-WSW-oriented Permo-Triassic rifting phase, the inherited brittle Caledonian fault network was repeatedly reactivated (Faleide et al., 2008). This rifting stage controlled the evolution of the North Sea and the proximal parts of the Vøring margin. (Fig. 1). A quiescent post-rift phase ensued and lasted from the Middle Triassic to the Early Jurassic, when the depositional environment in the area changed from marine to coastal (Gernigon et al., 2020). In the Early and Middle Jurassic, intermittent and moderate episodes of E-W crustal stretching occurred (Scheiber and Viola, 2018; Gernigon et al., 2020), leading to the initial development of the Møre and Vøring margins (Fig. 1). The Late Jurassic–earliest Cretaceous

rifting event is related to the northward propagation of the Atlantic rifting (Lundin and Doré, 2011), when bulk extension shifted to a NW-SE direction and the final opening direction was roughly perpendicular to the present-day coastline (Doré et al., 1999). During this phase, crustal stretching and pervasive faulting created space to accumulate significant Cretaceous syn-rift deposits (Osmundsen and Péron-Pinvidic, 2018; Zastrozhnov et al., 2020; Osmundsen et al., 2021).

During the Cretaceous, the large and deep Møre and Vøring basins formed in the distal part of the MNPM (Fig. 1, Blystad, 1995; Zastrozhnov et al., 2020). Both tectonic and thermal subsidence led to the accumulation of up to 8 km thick sedimentary successions in local depocenters. From the Late Cretaceous, the Møre Basin was subjected to thermal subsidence and passive sedimentation without any significant tectonism (Osmundsen and Péron-Pinvidic, 2018; Osmundsen et al., 2021). The Vøring Basin, instead, experienced renewed extension in the Late Cretaceous (Zastrozhnov et al., 2018; 2020; Osmundsen et al., 2021). The final breakup of the NE Atlantic Ocean initiated at 58-57 Ma in the Møre segment of the margin and later propagated northward to the outer Vøring Margin at 56-55 Ma (Ren et al., 2003; Gernigon et al., 2020; Zastrozhnov et al., 2020). Finally, compressional events affected the Vøring Basin from the Eocene to the Pleistocene as indicated by local basin inversion structures and partial reactivation of the faults bordering the many structural highs of the area (Lundin and Doré, 2002; Doré et al., 2008; Zastrozhnov et al., 2020).

The investigated areas include the islands of Hitra, Frøya, and Smøla and the Stad area onshore Norway, located at the transition between the NE-SW oriented MNPM and the N-S oriented North Sea margin (Fig. 1). In the northern MNPM, the islands of Hitra and Smøla consist of the 450-428 Ma granitic to granodioritic Smøla-Hitra batholith (Gautneb and Roberts, 1989),

attributed to the Upper Allochthon of the Norwegian Caledonides (Fig. 1). The batholith is overlain by Late Silurian-Devonian sandstone and conglomerate exposed along the southeastern coast of Hitra. On the northern part of Hitra and on Frøya, micaschist and foliated migmatite of the Uppermost Allochthon are exposed. In the Stad area, the tip of Kråkenes peninsula is composed of a gabbroic enclave within the WGR (*cf*. Krabbendam et al., 2000).

2.1 The Møre-Trøndelag Fault Complex (MTFC)

The regional-scale, ENE-WSW Møre-Trøndelag Fault Complex (MTFC) extends onshore for more than 300 km in mid- and western Norway before it enters the Norwegian Sea (Fig. 1; Gabrielsen et al., 1999; Redfield et al., 2005; Nasuti et al., 2012). This structure has been related to similarly oriented faults in the Scottish Highlands, such as the Highland Boundary Fault (e.g., Fossen, 2010). In the offshore domain, it separates the Jurassic–Cretaceous North Sea basin system to the south from the wider and deeper Cretaceous basins of the MNPM to the north (Fig. 1; Redfield et al., 2005). Onshore, the MTFC crosscuts the Precambrian autochthonous basement and the overlying Caledonian nappes (Braathen et al., 1999, 2002; Osmundsen et al., 2005; Corfu et al., 2014).

The MTFC is a composite fault complex consisting of different subvertical fault strands (e.g., Hitra–Snåsa Fault, Verran Fault), and an enveloping volume of rock deformed by second-order fault zones (Séranne, 1992; Braathen et al., 1999, 2002; Redfield et al., 2004, 2005; Osmundsen et al., 2005, 2006; Redfield and Osmundsen, 2009). The main fault strands are defined by a several meter thick mylonitic core, superimposed by brittle fault rocks (Kendrick et al., 2004). The MTFC has been repeatedly reactivated in response to stress regimes varying through time, resulting in a complex finite deformation pattern (e.g., Séranne, 1992; Gabrielsen et al., 1999;

178 Redfield et al., 2005; Osmundsen et al., 2006; Nasuti et al., 2011). A possible initial dextral
179 transpression has likely been accommodated by the MTFC in pre-Devonian times (Séranne,
180 1992). However, overall sinistral ductile Early to Middle Devonian shear is recorded by up to 2
181 km thick mylonitic shear zones, as documented by $^{40}Ar/^{39}Ar$ dating of synkinematic white micas
182 (Kendrick et al., 2004). From the Devonian onward, progressive regional exhumation led to the
183 transition into a shallower, brittle deformation regime. Previous studies propose multiple oblique
184 reactivations of the MTFC during the Late Devonian, Permo-Triassic, and Jurassic (e.g., Grønlie
185 and Roberts, 1989; Grønlie et al., 1991; Séranne, 1992; Sommaruga and Bøe, 2002; Redfield et
186 al., 2004, 2005). Pseudotachylytes from the Hitra-Snåsa Fault have been dated by $^{40}Ar/^{39}Ar$
187 laserprobe to the Late Carboniferous-Early Permian by Sherlock et al. (2004). Additionally, the
188 MTFC experienced normal faulting in the Middle to Late Jurassic–Early Cretaceous, as well as
189 possible Quaternary post-glacial reactivation (Sommaruga and Bøe, 2002; Redfield et al., 2005).
190 The area is still seismically active in an oblique-normal mode (Gabrielsen and Færseth, 1988;
191 Bungum et al., 1991).

192 # 3. MATERIALS AND METHODS

193 We carried out a multidisciplinary and multiscalar study to better constrain the brittle evolution
194 of the MNPM in space and through time. Our approach includes the remote sensing of bedrock
195 lineaments, field structural and microstructural analysis, paleostress inversion, and radiometric
196 K-Ar dating coupled with the detailed mineralogical characterization of selected fault rocks. In
197 the following we provide details of the used methodologies.

198 ## 3.1 Remote Sensing Lineament Detection

Lineament mapping was performed manually on a grayscale hillshaded Digital Elevation Model (DEM) of the onshore MNPM obtained from high-resolution (1m/pixel) airborne-LiDAR (Light Detection And Ranging) surveys. Grayscale hillshade DEMs with an illumination direction from the NW were used to map the lineaments. Lineaments were mapped at the 1:10.000 and 1:100.000 scales to test the regional significance of local (smaller scale) fracture patterns. The mapped lineaments are regarded as representing the surface expression of fault and fracture zones (*cf.* Gabrielsen and Braathen, 2014; Scheiber et al., 2015). To this purpose, mapping was assisted by and compared with available geological and topographic maps of the region to prevent tracing ductile foliations and shear zones and artificial lineaments (e.g., roads, fences). The strike of the mapped lineaments is displayed in rose diagrams computed with the MARD (Moving Average Rose Diagram) application by Munro and Blenkinsop (2012).

3.2 Structural Analysis

Field structural analysis focused on the easily accessible coastline of the MNPM, from Hitra in the north to the Stad area in the south (Fig. 1). Fieldwork was used to ground truth the remotely detected lineaments. 86 different structural sites from selected key areas of the MNPM were studied by systematically collecting fault-slip data, including information on fracture or fault orientation, slip direction and sense of movement, lithotype, fault rock type, and fracture mineralogy. In some cases, throw and spatial persistence/extension could also be were measured. This fault-slip dataset represents the input data for our paleostress inversion.

In addition, oriented thin sections of selected fault rock samples, cut parallel to the transport direction (fault slip lineation) and perpendicular to the fault plane, were prepared for optical microscopy and petrographic analysis.

3.3 Paleostress Inversion

Paleostress inversion analysis is useful to reconstruct the orientation of the stress field that caused slip along a given homogeneous set of cogenetic faults. When studying a multiply reactivated and complexly deformed area, paleostress inversion analysis can ideally help to distinguish and reconstruct how the stress field orientation varied through time, during different deformation events. In our study, the collection of fault-slip data included the fault plane orientation, the slip direction and the sense of slip (normal, reverse, dextral or sinistral). Kinematic analysis relied on the growth direction of slickenfibers behind slickensides, Riedel shears and small-scale pull-apart structures (e.g., Hancock, 1985; Petit, 1987).

Starting from the fault-slip data, paleostress inversion calculates the reduced stress tensor that best accounts for an internally homogeneous set of faults. This approach is based on the following assumptions (e.g., Wallace, 1951; Bott, 1959; Twiss and Unruh, 1998; Pollard, 2000; Lacombe, 2012; Lacombe et al., 2013): 1) the observed slip direction is parallel to the maximum shear stress resolved on the fault plane; 2) the faulted volume of rock is physically homogeneous and isotropic; 3) the faulted rock volume has to be large compared to the dimension of the studied faults and a homogenous stress distribution therein is necessary; 4) the studied medium responds to the applied stresses as a rheologically linear material; 5) faults do not mutually interact, and 6) no block rotation occurred at the time of faulting. These assumptions still represent oversimplifications of the complexity of faulting in natural systems and by accepting them we necessarily introduce uncertainties in any paleostress analysis. Moreover, they are only seldomly met when studying complexly fractured basements, where the finite fault and fracture pattern derives from multiple and thus superimposed faulting events. This may result in reduced stress tensors whose definition and interpretation are dubious.

On the other hand, all these uncertainties notwithstanding, several studies have shown that it is possible to obtain consistent paleostress reconstructions even in multiply deformed metamorphic terrains by acquiring a large dataset, carefully sorting statistically fault populations and by validating the results against independent constraints (e.g., Viola et al., 2009; Saintot et al., 2011; Mattila and Viola, 2014).

When dealing with multiple faulting events, the identification of internally consistent subsets of faults separated from the total and heterogeneous available dataset is a fundamental step. A homogeneous set of faults is defined as a group of faults and fractures in any given area that can be genetically bundled together because they formed in response to the same stress field and, as such, they are compatible from a geometric, kinematic and dynamic perspective and have similar fault rock assemblages and mineral coatings. In this study, observations from remote sensing, field constraints and microstructural analysis were considered to sort the total fault-slip dataset into internally consistent subsets of faults from along the studied margin.

The individual fault sets were analyzed using the WinTensor software (Delvaux and Sperner, 2003) to obtain their reduced stress tensors. This software iteratively applies an inversion algorithm to search for the state of stress that best accounts for the input fault-slip dataset (e.g., Angelier, 1984; Delvaux and Sperner, 2003). The robustness of the optimization process is measured by the fit between the theoretical slip vectors and those measured in the field (Delvaux and Sperner, 2003). This is achieved by analyzing for all faults in a set the misfit angle α, which is defined as the acute angle between the theoretical maximum shear traction vector and the measured slip vector for an individual fault plane. A set of faults can be considered as homogeneous if the slip deviation (the α value) is lower or equal to 30°, a condition that implies that all processed faults are compatible with the calculated stress tensor. If the α value for a given

fault is greater than 30°, then that fault is incompatible with the computed reduced tensor, suggesting that it belongs to a different set and that it formed in a different stress field and, thus, during a different deformation episode (Delvaux and Sperner, 2003).

The calculated reduced stress tensor is defined by the orientation of the three main compressional stress axes (σ_1, σ_2, and σ_3, with $\sigma_1 \geq \sigma_2 \geq \sigma_3$) and by the stress ratio R ($R = (\sigma_2 - \sigma_3)/(\sigma_1 - \sigma_3)$) (Angelier, 1984; Lacombe, 2012). To express in a clearer way the stress ratio and the resulting stress regime, we rely on the R' index, which is calculated by R' = R, when σ_1 is vertical (extensional stress regime), R' = 2 – R, when σ_2 is vertical (strike-slip stress regime) and R' = 2 + R, when σ_3 is vertical (compressional stress regime; Delvaux and Sperner, 2003). R' ranges from 0 to 3. R' = 0.5 describes a pure extensional regime, R' = 1.5 describes a pure strike slip regime and R' = 2.5 indicates a pure compressional regime. All the intermediate values indicate a mixed regime, e.g., R' = 1.0 translates to a transtensional regime.

In summary, the reduced stress tensors presented in this study describe paleostress regimes inverted from different, manually sorted sets of faults from along the margin. The obtained paleostress regimes are correlated with specific tectonic events in the regional framework experienced by the MNPM.

3.4 K-Ar Radiometric Dating of Fault Rocks Coupled with Mineralogical Analysis

K-Ar radiometric dating and X-ray diffraction (XRD) were performed on twelve fault gouges and one non-cohesive altered rock at the laboratories of the Geological Survey of Norway (Trondheim, Norway) following the procedure described by Viola et al. (2018). Collected fault rock samples are representative of the main trends of structural lineaments defined by remote sensing analysis. Each sample was disintegrated by repeated freezing and thawing cycles to

avoid mechanical grain size reduction of coarse-grained minerals and their contamination in the finer fractions. Samples were, then, separated into five grain size fractions (<0.1, 0.1-0.4, 0.4-2, 2-6 and 6-10 μm). The <2, 2-6 and 6-10 μm grain size fractions were separated in distilled water using Stokes' law, whereas the finer fractions (<0.1, 0.1-0.4 and 0.4-2 μm) were concentrated by high-speed centrifugation of the <2 μm fraction. The mineralogical composition of each grain size fraction was determined by XRD analysis (with a Bruker D8 Advance diffractometer). Mineral quantification was carried out on randomly prepared specimens using Rietveld modelling with the TOPAS 5 software. The lower limit of quantification and accuracy are mineral-dependent but are generally 1 wt% and 2-3 wt%, respectively. For further details, the reader is referred to Viola et al. (2018) and Tartaglia et al. (2020).

4. RESULTS

4.1 Bedrock Lineament Pattern

The results of the manual extraction of bedrock lineaments from the coastal area of the MNPM at the 1:100.000 (Fig. 2a) and 1:10.000 scales (Fig. 2b, c) show that lineaments can be grouped into four main sets:

i) (E)NE-(W)SW lineaments, largely parallel to the coastline and to the MTFC;
ii) NNW-SSE lineaments;
iii) WNW-ESE lineaments;
iv) E-W lineaments.

The (E)NE-(W)SW oriented trend is dominant and particularly evident on Hitra and Smøla (Fig. 2b), where one of the strands of the MTFC, the Hitra-Snåsa Fault, is well exposed.

When comparing the rose diagrams obtained from the two different scales at which the remote sensing was carried out, some differences can be recognized. This reflects the number of picked lineaments, which is generally one or two orders of magnitude greater at the 1:10.000 scale than at the smaller scale (Fig. 2). Despite the different number of mapped lineaments, however, the same main trends emerge from both mapping scales, with some exceptions for the Runde and Kråkenes areas. The 1:100.000 scale lineament trends in the Runde area are oriented NNW-SSE, NNE-SSW and ENE-WSW (Fig. 2a). The ENE-WSW lineaments define the main trend in the 1:10.000 scale stereoplot of the Runde area (Fig. 2c), but the NNW-SSE oriented lineaments are less abundant than at the 1:100.000 scale (Fig. 2a). A similar situation is evident in the Kråkenes area, where the distinct WNW-ESE lineament trend derived from the 1:100.000 scale is less abundant at the 1:10.000 scale (Fig. 2a, c). This observation could indicate that NNW-SSE and WNW-ESE lineaments tend to be better expressed at smaller scale because they represent older, regional structural trends. Their abundance at the 1:10.000 scale could also be relatively smaller in comparison to the great number of variably oriented faults and fractures recorded and mapped at this scale.

The mapped lineaments exhibit crosscutting relationships that can be summarized as follows (Fig. 3): WNW-ESE trending lineaments show mutual crosscutting relationships with all the detected trends. In the area of Hitra, the ENE-WSW lineaments are persistent and seem to cut all other lineaments, even if they are locally crosscut by NNW-SSE and NE-SW trends. NNW-SSE and NE-SW trending lineaments are generally crosscut by all the detected trends, and locally, NE-SW trending lineaments crosscut the NNW-SSE lineaments. According to these results, ENE-WSW striking lineaments thus appear to be the youngest, or the ones that have been reactivated more recently, and the NNW-SSE and NE-SW the oldest.

4.2 Mesostructural Brittle Fault Characterization

The structural stations studied along the MNPN are shown in Figure 4a. Faults and fractures at the studied sites cut across different types of rock. The host rocks along the MNPM are mainly represented by granitic and granodioritic gneiss of the WGR, Devonian sandstone and conglomerates, micaschist, foliated migmatite and locally eclogitic lenses.

The collected fault-slip data have variable strike and dip. The associated striae are also variably oriented, indicating both dip-slip, predominantly with normal kinematics, and, to a lesser extent, strike-slip faulting. Faults locally rework and exploit inherited ductile planar fabrics, mainly the mylonitic foliation (Fig. 5a). On the island of Jøsnøya, south of Hitra, high-angle conjugate sinistral ENE-WSW and dextral NE-SW oriented fault planes are exposed. The sinistral ENE-WSW high-angle faults rework the mylonitic fabric (Fig. 5a). The strikes of these faults are parallel to the main remotely detected lineament set in the area. These faults reactivate the mylonitic planar fabric and are systematically cut by high angle NNW-SSE trending normal faults (Fig. 5b). These normal faults are locally decorated by fine-grained epidote mineral coatings. Also, the strike slip faults on Jøsnøya are, in turn, cut by younger calcite veins.

Brittle fault zones along the margin are associated with a broad range of fault rock assemblages. In highly fractured fault cores, fine-grained cataclasite is associated with or crosscut by distinct layers of clay-rich fault gouges (Fig. 5c, d). Due to the lack of marker horizons in the study area, the amount of displacement along individual faults remains largely unknown. Locally, along some brittle structures, the host rock is dismembered, and appears as unconsolidated coarse-grained material. In these fault and fracture zones, the mostly granitic or gabbroic host rock is altered.

Brittle structures along the MNPM exhibit different mineralogical coatings, including epidote, chlorite, calcite, and quartz, sometimes decorating the same plane but also crosscutting and overprinting each other, forming a complex multilayered arrangement of fault rocks. Epidote coatings on faults and fractures are generally reworked and/or cut by younger, few mm-thick, milky white prehnite veins (Fig. 5e). Calcite occurs as mm-thick striated synkinematic coating on the fault planes (Fig. 5f), as variably thick veins, or secondary, coarse-grained, post-kinematic fracture infill.

The studied fault and fracture planes have been classified according to their mineralizations and plotted in rose diagrams (Fig. 4b). Green, ultrafine-grained, epidote coatings are mainly associated with c. N-S trending faults but are also locally present on differently oriented faults (Fig. 4b). Fine-grained quartz mineralizations and quartz veins show a similar pattern but are particularly abundant on E-W striking faults. Red iron oxide coating mainly occurs on WNW-ESE striking faults (Fig. 4b). Milky white, extremely fine-grained, mm to cm thick prehnite coating is mainly associated with roughly N-S and NNW-SSE striking faults. Dark blue/green, mm-thick, chlorite coating does not display any preferential orientation. Calcite is present on all sets of fractures and faults, irrespective of their orientation, but shows a predominance along N-S striking brittle structures (Fig. 4b).

4.2.1 Fault Zone K-Ar Dating

Twelve fault gouges and one altered rock were sampled for radiometric K-Ar dating. The details of the sampled fault zones are reported in Table 1 and Figure 6. The sampled fault gouges belong to three main sets of faults: i) low-angle (W)NW-(E)SE striking fault planes (samples 19.006B, 19.078, and 19.016; Fig. 6a-c); ii) variably dipping, ENE-WSW oriented faults (samples

19.007A, 19.011, 19.042A, GT18_01/2; Fig. 6d-i); iii) medium to high-angle, oblique and dip-slip, NNE-SSW oriented faults (samples 19.030A, 19.049, 19.070, 19.076; Fig. 6j-m). Samples are from different rock types (Table 1), mainly granitic and gabbroic rocks (19.006B, 19.007A, 19.016, 19.030A, 19.042A/E, 19.078), migmatite (19.049) and amphibolite or gneiss (19.011, 19.070, 19.076, GT18_01, GT18_02).

Some of the sampled fault zones contain a complex assemblage of different fault rocks within the core with different generations of fault gouges, cataclasites and veins. The low-angle N-dipping fault of sample location 19.006B (Fig. 6a), for example, contains a 7 cm thick fault gouge layer associated with a subparallel blocky calcite vein. The NNE-dipping fault at location 19.016 contains a layer of gouge associated with subparallel veins of calcite and zeolite (Fig. 6c). Fault zones 19.078 and 19.011 are composed of a few cm thick fault gouge layer (Fig. 6b, e).

Samples 19.042A and E are from an ENE-WSW striking strike-slip fault and are from two different structural levels (Fig. 6f, g). In the lower part of the outcrop, a grey, very plastic fault gouge is exposed (sample 19.042A), whereas the upper part of the same brittle structure is filled with altered/weathered sandy granite (sample 19.042E).

Samples 19.030A and 19.049 are from SE-dipping fault zones; both their fault cores are composed of a c. 3 cm thick layer of cohesive fine-grained cataclasite, chunks of blocky calcite veins and the sampled fault gouge (Fig. 6j, k). The reddish fault gouge of the ENE-WSW striking fault at locality 19.007A also embeds calcite veins (Fig. 6d).

Samples GT18_01 and GT18_02 were collected from the same c. 7 m thick fault zone on the island of Runde (Fig. 6h). They are from two distinct generations of gouge, with GT18_01

cutting across GT18_02. The two gouge layers have different angle of dip, where the younger gouge layer (GT18_01) has a steeper dip (Fig. 6i).

Finally, some brittle fault zones exploit inherited ductile planar fabrics. For example, NNE-SSW striking mylonitic shear zones were reworked by brittle faulting (e.g., samples 19.070 and 19.076; Fig. 6l, m).

4.3 Microstructural Data

Eight samples of cataclasite were collected from outcrops of representative fault zones at the investigated structural sites (Fig. 4a) for microstructural characterization. Although the collected samples cannot be considered representative of the entire population of faults along the margin, their analysis allows us to derive structural and mineralogical inferences as to the conditions of deformation and to define systematic and mineralogically-constrained crosscutting relationships. Microstructural analyses focused on: (i) the identification of the mineralogy and microstructure of different mineral coatings observed in the field; (ii) the identification of overprinting relationships between different coatings and thereby (iii) deducing a temporal sequence of deformation events.

Our study revealed a systematic sequence of overprinting relationships between veins and cataclastic layers characterized by specific mineral phases. From the oldest to the youngest, this sequence is defined by the following evidence:

(i) Protocataclasites are generally pervasively fractured and characterized by the occurrence of (coarse-grained) epidote mineralizations (Fig. 7a). Multiple events of fracturing and precipitation of epidote-bearing mineralizations are inferred from the

occurrence of epidote-bearing cataclasites with remarkably different grain size and crosscutting relationships (e.g., Ep_1, Ep_2 and Ep_3 in Fig. 7a).

(ii) Quartz veins and quartz-rich cataclasites of variable grain size dissect the epidote-bearing cataclasites (Fig. 7b). Several generations of quartz veins and quartz-rich cataclasites can be identified (e.g., Qtz_1, Qtz_2 in Fig. 7b).

(iii) Prehnite-bearing veins and cataclastic layers cut across and disrupt the quartz- and epidote-bearing cataclasites described above (Fig. 7c-d). Quartz- and epidote-layers are observed as mm-size clasts embedded within prehnite veins and cataclastic layers.

(iv) Fine-grained cataclasites of mixed mineralogical composition containing large clasts of epidote-, quartz-, and prehnite-bearing cataclastic layers and veins (Fig. 7e).

Fault gouges are commonly associated with calcite mineralization and subordinated red iron oxides and quartz (Table 1). Calcite-bearing mineralizations can be coarse-grained (mm-size) and are locally associated with euhedral zeolite (Fig. 7f).

4.4. Paleostress Inversion

The total analyzed fault-slip dataset was subdivided into heterogeneous subsets according to a geographic position criterion in order to obtain subsets not exceeding 350 fault-slip data each, which are more easily handled. Inversion was then applied to fault-slip data subsets that were defined based on the criteria explained above, aiming at the identification of internally consistent data according to field constraints, fault orientation, kinematics, and fault characteristics, such as specific mineralization (quartz, epidote, calcite, chlorite), or a specific area with a given geological feature (occurrence of foliation, type of protolith, etc.).

Each obtained dataset was inverted, and initial results were progressively refined by discarding faults with misfit angles >30°. The inversion procedure was reiterated until stable results were obtained (see also Scheiber and Viola, 2018). As this approach was applied iteratively, fault-slip data of potentially cogenetic faults were tested against their geometric and kinematic compatibility and, in case the misfit angle did not exceed 30°, included into the final dataset to be inverted. Faults without any recorded mineralization were also tested for their compatibility with the calculated stress field. By such an approach, we identified similar stress fields for the different subareas, which stresses the regional significance of the obtained stress regimes. Among them, the most recurrent are shown in Figure 8 from older to younger.

A pure compressional stress regime with the maximum horizontal compressional stress axis (σ_1) oriented NW-SE was obtained by the inversion of low angle N-dipping faults (R': 2.54), that invariably containing brittle fault rocks in their cores (Fig. 8a). Some of these faults are reverse, while other faults recorded a later extensional reactivation.

Pure compression was followed by a transpressional stress regime (R':1.98) with σ_1 oriented NW-SE, which formed conjugate strike-slip faults, oriented NW-SE (sinistral) and E-W (dextral), invariably decorated by epidote and chlorite (Fig. 8b).

A well recorded stress regime along the entire MNPM is an extensional stress field with σ_3 oriented E-W (R':0.37; Fig. 8c). It generated NNE-SSW and NNW-SSE normal faults and reactivated some NW-SE oblique fault planes. This stress field is recorded by fault zones mainly decorated by epidote and quartz coatings, and subordinately exposing brittle fault rocks in their cores.

461 The last two inverted stress regimes reactivated variably oriented faults and fractures inherited
462 from the previous deformation episodes. An extensional field with σ_3 oriented NW-SE
463 reactivated faults and fractures decorated by prehnite, quartz, zeolite and calcite coatings (R':
464 0.52; Fig. 8d). Finally, prehnite decorated faults and/or associated with brittle fault rocks,
465 oriented NE-SW and NW-SE formed or were reactivated by an extensional stress regime with σ_3
466 oriented WNW-ESE (R': 0.24, Fig. 8e).

467 **4.5 K-Ar Data**

468 The twelve sampled fault rocks and the altered rock were characterized mineralogically by XRD
469 analysis and dated by the K-Ar method. The XRD data are not always quantitative, because of
470 the little amount of material recovered from some of the samples (Table 2). The
471 (semi)quantitative XRD data show that in the different samples the percentage of clay minerals
472 (smectite, illite/muscovite, vermiculite, and palygorskite) increases with decreasing grain size
473 (Table 2, Fig. 9), such that the analyzed < 0.1 μm grain size fraction of all the samples only
474 comprise clay minerals (Fig. 9). The amount of quartz, K-feldspar, plagioclase, epidote,
475 amphibole, calcite, zeolite (when present) generally decreases with decreasing grain size.
476 Generally, the chlorite content also decreases with decreasing grain size and is accompanied by
477 an increase of the smectite content. Focusing on the K-bearing phases, the finer grain size
478 fractions are invariably enriched in K-bearing clay minerals, such as illite, illite-smectite mixed
479 layers and illite-vermiculite (Fig. 9). K-feldspar is not present in all the samples, but when
480 present, its amount decreases progressively and is absent in the finest grain size fraction (Fig. 9,
481 Table 2).

The sixty-two new K-Ar data obtained from twelve fault gouges and one altered granitic rock sample range from 848 ± 11 to 71 ± 1 Ma (Table 3). The ages are plotted on an "Age vs. grain size fraction" diagram (Fig. 10). However, sample 19.049 did not contain sufficient material for dating of grain sizes <0.4 μm, and samples 19.016 and 19.042E did not contain sufficient material for dating of the finest (<0.1 μm) grain size fractions. The graph shows inclined curves with a common trend: coarser grain size fractions have older ages while the younger ages are associated with the finest fractions. The K-Ar ages of the finest grain size fractions (< 0.1 μm) are 197 ± 3, 176 ± 2, 138 ± 3, 130 ± 3, 126 ± 3 (twice), 91 ± 3, 86 ± 1, 80 ± 1 and 71 ± 1 Ma (Table 3).

5. DISCUSSION

The complex network of lineaments with different orientations along the MNPM, the abundance of brittle structures and the high variability of mineralogical assemblages within the studied faults and fractures document the polyphase brittle evolution experienced by the MNPM. Despite its long and, at times, convoluted history, our systematic approach contributes to unravelling its deformation and adds new temporal constraints to its polyphase evolution.

5.1 Fault Rock Mineral Assemblages

The sequence of mineral coatings established for the analyzed fault cataclasites constrains a progressive evolution of retrograde cooling of the MNPM, presumably from the Carboniferous onward. Indeed, the epidote + chlorite (+ quartz) assemblage observed in the oldest cataclasite generations suggest deformation conditions close to the frictional-viscous transition in the continental crust under sub-greenschist facies conditions (T ≤275 °C; e.g., Wehrens et al., 2016).

This mineral assemblage occurs in several generations of coherent (ultra-)cataclasite (Fig. 7a), suggesting recurrent events of brittle fracturing, fluid infiltration and mineralization precipitation and cataclasis. The mixed mineralogical composition and prehnite-bearing cataclasites indicate the continuation of brittle cataclasis and fluid infiltration processes at lower temperatures at which prehnite becomes stable ($T \approx 200\text{-}250$ °C; e.g., Malatesta et al., 2021). More than the other described mineralization types, quartz- and prehnite-bearing cataclasites exhibit evidence of fluid-overpressure and vein formation, preserving several generations of both comminuted and euhedral quartz and prehnite crystals (Fig. 7c). Furthermore, gouge-bearing faults are commonly associated with calcite and zeolite mineralizations. Unpublished clumped isotope thermochronological data on calcite veins from the studied faults constrain calcite growth temperatures between c. 190 and 30 °C (Tartaglia, 2021). These temperature estimates are in line with zeolite formation temperatures, commonly well below 200 °C (Weisenberger and Bucher, 2010). The preservation of coarse euhedral crystals of both calcite and zeolite (Fig. 7f) may indicate that these veins overprint and post-date the latest stages of brittle faulting and gouge formation.

All in all, this sequence of mineralogical assemblages within the studied fault rocks supports a general cooling trend throughout the brittle evolution of the MNPM. However, the lack of a clear systematic relationship correlating fault strike and fault mineralogy (or sequence of mineral assemblages; see Section 5.2 below, Fig. 8) does not allow us to retrieve general conclusions at the scale of the MNPM. Nevertheless, the mineral paragenesis coupled with K-Ar data from fault zones may provide local, but valuable constraints on the thermal and temporal evolution of the brittle deformation history.

5.2 Absolute Dating of MNPM Faults

526 The obtained inclined “age vs. grain size” curves (Fig. 10) are interpreted as recording variable
527 degrees of physical mixing between authigenic and synkinematic mineral phases and inherited
528 protolithic minerals, and/or mixing of different generations of authigenic minerals (van der
529 Pluijm et al., 2001; Verdel et al., 2012; Torgersen et al., 2015; Viola et al., 2016; Vrolijk et al.,
530 2018). This interpretation is in accordance with the “Age Attractor Model” by Torgersen et al.
531 (2015), wherein the amount of authigenic and synkinematic K-bearing phases progressively
532 increases with decreasing grain size. The finer grain size fractions are, therefore, enriched in
533 synkinematic, authigenic minerals (van der Pluijm et al., 2001; Zwingmann and Mancktelow,
534 2004). However, they may still include inherited protolithic minerals or different generations of
535 K-bearing authigenic phases reworked during multiple stages of deformation, such that the ages
536 obtained from the finest grain size fractions are still to be considered as maximum ages. At the
537 same time, the ages yielded by the <0.1 μm grain size fractions represent the best available
538 constraint on the absolute timing of the most recent faulting event recorded by the studied fault
539 rock (van der Pluijm et al., 2001; Zwingmann and Mancktelow, 2004; Torgersen et al., 2015;
540 Viola et al., 2016, Tartaglia et al., 2020). Within fault rocks, authigenic mineral formation occurs
541 because faulting is a dilatational process that enhances fluid ingress and promotes the (re)-
542 crystallization of synkinematic mineral phases. However, also post-tectonic fluid infiltration
543 within a permeable fault core may lead to authigenesis and, therefore, to dates that do not reflect
544 the age of faulting. Careful fault rock characterization is, thus, necessary to ascertain the details
545 of faulting as preserved and constrained by the microstructure of the fault rocks and to be able to
546 produce a meaningful interpretation of the obtained K-Ar ages. The fact that the fault gouges
547 sampled in this study can be generally associated with the last faulting event experienced by the
548 sampled fault zones (as indicated by our multiscalar structural analysis) and that the obtained

549 ages are comparable to the timing of already known regional tectonic events (e.g., Fossen et al.,
550 2021; Osmundsen et al., 2021) suggests that the obtained K-Ar fault gouge dates are truly due to
551 synkinematic crystallization and not to post-tectonic authigenesis and or alteration due to later
552 fluid ingress.

553 The coarser grain size fractions can include protolithic, inherited minerals such as, for example,
554 K-feldspar from the host rock lithology. If several of the coarser grain size fractions from one
555 sample yield a statistically identical or similar age, it is reasonable to conclude that this age has a
556 geological significance (e.g., Viola et al., 2016; Vrolijk et al., 2018; Scheiber et al., 2019;
557 Tartaglia et al., 2020). The "Age Attractor Model" considers the intermediate grain size fractions
558 (0.1-0.4, 0.4-2 and 2-6 μm) as representing a mix of different (synkinematic and protolithic)
559 grains with varying isotopic signatures and they are, therefore, commonly devoid of a geological
560 meaning.

561 In the obtained K-Ar age vs. grain size plots, some age clusters are clearly recognizable (Fig.
562 10). The ages of the >2 μm grain size fractions of samples 19.006B, 19.049, 19.070 and of the
563 0.4-2 μm grain size fraction of sample 19.078 form a Carboniferous cluster with a mean age of
564 321 ± 8 Ma (MSWD=2.74). A Triassic/Jurassic mean age of 202 ± 6 Ma (MSWD=5.9) is
565 calculated from the age cluster constituted by the <0.1 μm finest grain size fraction of sample
566 19.006B, the coarsest 6-10 μm fraction of samples 19.007A, GT18_01 and GT18_02 and the >2
567 μm fractions of the samples 19.042E and 19.076. The ages of the intermediate fractions of
568 19.042E and GT18_01 and of the finest fractions of 19.042E and 19.078 yield a Jurassic cluster
569 with a mean age of 177 ± 12 (MSWD=0.1). The ages of the finest <0.1 μm grain size fractions of
570 samples 19.007A, 19.011, GT18_02, 19.076, and of the >0.4 μm fractions of sample 19.030A
571 define an Early Cretaceous cluster with a mean age of 122 ± 5 Ma (MSWD=3.5). Finally, three

572 <0.1 μm fraction ages are younger than 100 Ma (c. 71, 80, 86, 91 Ma), indicating an episode of
573 illite and smectite crystallization in the Late Cretaceous.

574 The finest grain size fractions, in addition to also some coarser fractions that define the age
575 clusters in the Late Triassic-Early Jurassic and Early and Late Cretaceous, are all composed of
576 authigenic K-bearing minerals, mainly k-bearing smectite, smectite-illite and illite-muscovite.
577 Therefore, they allow to constrain discrete faulting events through the synkinematic
578 (re)crystallization of K-bearing clay minerals. Two exceptions are the 6-10 μm grain size
579 fraction ages of samples 19.042A and GT18_01. In the case of sample 19.042A, the coarser
580 fraction ages show an oscillating trend, suggesting a mixing of protolithic and authigenic grains.
581 The age of its coarser grain size fraction thus remains devoid of an apparent geological meaning.
582 Sample GT18_01 was collected from the same fault zone as sample GT18_02. These two gouges
583 represent two different generations of fault rock, with GT18_01 cutting across GT18_02. Their
584 finest fraction ages (<0.1 μm), 71 Ma and 126 Ma for GT18_01 and GT18_02, respectively,
585 confirm the crosscutting relationship identified at the outcrop (Fig. 6i). Their coarser grain size
586 fractions yield the same age range (201 ± 3, 204 ± 4 Ma), suggesting that the two gouges derive
587 from a common Triassic "protolith", developed during a faulting or alteration event, and then
588 reactivated at different times during the subsequent brittle deformation history.

589 To summarize, the obtained K-Ar ages can be grouped into four significant clusters, which, from
590 older to younger, date to:

591 1) Carboniferous, with a mean age of 321 ± 8 Ma (MSWD=2.74);

592 2) Late Triassic-Jurassic with two distinct mean ages at 202 ± 6 Ma (MSWD=5.9) and at 177 ±
593 12 Ma (MSWD=0.1);

3) Early Cretaceous with a mean age of 122 ± 5 Ma (MSWD=3.5);

4) Late Cretaceous with ages between c. 91 and 71 Ma.

The Carboniferous cluster is constrained by only the coarser grain size fractions of the dated samples. Among the fractions yielding Carboniferous ages, only the coarser grain size fraction of sample 19.006B contains K-feldspar (3%) in addition to 14% illite/muscovite (Table 2, Fig. 9). The K-feldspar is presumably inherited from the granitic protolith and likely records the Upper Devonian-Carboniferous age of cooling during exhumation of the WGR (cf. Walsh et al., 2013). The other Carboniferous ages derive from illite-smectite mixed layers or illite/muscovite, which most probably formed during faulting. This Carboniferous age cluster possibly represents brittle activity along the MNPM during the initial stages of the Norwegian-Greenland Sea rifting (Rotevatn et al., 2018; Gernigon et al., 2020). More specifically, similar Carboniferous ages (c. 320 Ma) have been constrained by K-feldspar $^{39}Ar/^{40}Ar$ dating from a cataclastic granite in the hanging wall of the Høybakken Detachment, NE of Hitra (Kendrick et al., 2004). This result has been interpreted as recording the early stages of brittle transtension along the MTFC (Kendrick et al., 2004). A very similar K-Ar illite age (312 Ma) has also been documented from the onshore East Greenland rift system and interpreted as evidence of a Paleozoic rifting phase associated with Carboniferous faulting (Rotevatn et al., 2018). Additionally, similar Carboniferous ages have been reported in a study reporting a microstructurally controlled K-Ar dating approach by Scheiber et al. (2019) and, also, by Viola et al. (2016) farther south in coastal western Norway. In summary, the new results highlight early Carboniferous tectonic activity (likely transtensional, e.g., Kendrick et al., 2004; Osmundsen et al., 2021) onshore the MNPM. Also, Osmundsen et al. (2021) describe a “core-complex and basin” architecture for the proximal MNPM, arguing it to be the result of Late Paleozoic-Early Mesozoic tectonic activity (Osmundsen et al., 2021). It is

plausible that these structures formed during the Carboniferous. Finally, the Late Carboniferous ages are coeval also with the Late Carboniferous to Early Triassic Oslo rifting (Larsen et al., 2008; Fossen et al., 2021).

Although during the Triassic the offshore MNPM is known to have experienced a relatively quiescent period characterized by only moderate extension (Gernigon et al., 2020), our results indicate some Late Triassic activity. Thus, the c. 202 Late Triassic/Early Jurassic and the 177 Ma Jurassic mean ages possibly represent a distinct tectonic phase associated with crustal stretching during and/or slightly after the first rifting phase reported for the NE Atlantic (Gernigon et al., 2020).

Our 122 ± 5 Ma Early Cretaceous age may reflect onshore faulting related to the second rifting phase. In fact, in the Early Cretaceous extension is known to have occurred as recorded by movement along major boundary faults causing block rotation in the offshore MNPM, as well as the reactivation of the MTFC (e.g., Fjellanger et al., 2005; Osmundsen and Péron-Pinvidic, 2018). Finally, in the Late Cretaceous, a rifting episode is recorded in the outer Møre and Vøring basins. That rifting defined the pre-breakup setting with the structuring of the complex outer ridges and sub-basin system (Ren et al., 2003; Péron-Pinvidic et al., 2013). However, in the Late Cretaceous the proximal offshore domain is generally described as quiescent (Péron-Pinvidic et al., 2013; Gernigon et al., 2020) Thus, the obtained < 100 Ma Late Cretaceous ages could reflect later reactivation of onshore suitably-oriented faults, due to the later stages of rifting prior to the final breakup of the NE Atlantic Ocean (Gernigon et al., 2020). Similar ages have been reported by other authors onshore along the North Sea Margin (Tartaglia et al., 2020; Fossen et al., 2021 and references therein).

639 ### 5.3 Brittle Evolution through Time

640 Our study has allowed us to define and characterize the main trends of the brittle structural grain
641 along the MNPM by remote sensing at the 1:10.000 and 1:100.000 scales and field work ground
642 truthing. In order to obtain a comprehensive evolutionary model of the brittle deformation
643 history recorded by the MNPM, the obtained structural and mineralogical data coupled with the
644 K-Ar ages interpreted as geologically meaningful, are discussed for each set of brittle structures,
645 subdivided according to their orientation. Moreover, a radial plot of structural data vs. obtained
646 K-Ar ages is shown in Figure 11 and described in the following paragraphs.

647 #### *5.3.1 NE-SW and NNW-SSE Striking Faults*

648 The NE-SW and NNW-SSE striking lineaments are very common along the MNPM. By remote
649 sensing, these lineaments appear to be the oldest structural features, as they are generally cut the
650 other lineament trends (Fig. 3). Most of the NE-SW and NNW-SSE faults and fractures
651 accommodate normal and transtensional kinematics. They are decorated by quartz, epidote,
652 chlorite, calcite, prehnite, and commonly contain fault rocks such as fine-grained cataclasite and
653 distinct layers of fault gouge.
654 The complex arrangement of cataclastic layers and mineral coatings (see Fig. 5e) derives mainly
655 from this set of faults. They mainly contain epidote cataclasites dissected by quartz veins and by
656 later thin prehnite cataclastic layers (Fig. 7).
657 Four dated samples belong to this set of lineaments (Fig. 11). Their K-Ar ages of the <0.1 μm
658 grain size fractions are Early and Late Cretaceous. The coarser grain size fractions consisting of
659 illite-smectite mixed layers and illite yield Carboniferous, Triassic, and Early Cretaceous ages
660 (Fig. 11). These radiometric data, the widespread occurrence in the field of the NE-SW and

NNW-SSE striking faults and their variability in mineralogical coatings suggest that this set of faults recorded several brittle deformation events affecting the margin from the Carboniferous down to the last documented reactivation in the Late Cretaceous.

The NE-SW and NNW-SSE striking faults are geometrically and kinematically compatible with a transpressional stress regime with σ_1 oriented NW-SE, which formed epidote and chlorite mineralizations. Additionally, they could be reactivated during the NW-SE extensional stress regime characterized by prehnite, quartz and calcite mineralizations. Some of these faults may thus have exploited a preexisting Caledonian fabric, prior to their own repeated reactivation and reworking during rifting due to their geometrical compatibility with the extensional stress fields.

5.3.2 ENE-WSW Striking Faults

The ENE-WSW striking lineaments are parallel to the northern part of the MNPM coastline, specifically the trend of the MTFC. They are particularly abundant on the island of Hitra, where the main strand of the MTFC, the Hitra-Snåsa Fault, is exposed (Redfield et al., 2005, 2009). Remote sensing analysis indicates that this trend generally cut all the other detected trends, in particular in the area of Hitra. The radiometric dating of our selected ENE-WSW striking fault zones (Fig. 11) indicates that these faults have recorded brittle events along the MNPM ranging from the Late Triassic to the Late Cretaceous. The oldest radiometric age of this set of faults is Late Triassic (201 ± 3 Ma, GT18_01, Table 3).

The ENE-WSW striking faults have a variable dip and accommodate strike-slip (mainly sinistral) or normal kinematics. They are mainly associated with chlorite and iron oxide mineralizations and locally with epidote and prehnite. These faults are geometrically compatible with the E-W and NE-SW extensional regimes experienced by the MNPM (Fig. 8). The high angle ENE-WSW

683 striking faults are generally localized along the MTFC mylonitic foliation. According to their
684 radiometric ages, these studied faults record only the evidence of the brittle deformation due to
685 the multiphase rifting of the NE Atlantic. However, pre-Triassic activity along the ENE-WSW
686 faults, parallel to the MTFC, cannot be excluded. Potential evidence is to be found in the
687 presented crosscutting relationships at the macroscale, the absolute dating of strands of the
688 MTFC as Devonian and Late Carboniferous-Early Permian (e.g., Kendrick et al., 2004; Sherlock
689 et al. 2004), as well as in the offshore ENE-WSW-trending lineaments bounding pre-middle
690 Triassic strata in the Froan basin (Osmundsen et al. 2021). Indeed, ENE-WSW striking fault
691 patterns in the area have been previously interpreted as Riedel-shears related the main branches
692 of the MTFC (Hitra- Snåsa and Verran Faults), resulting from sinistral strike-slip tectonics
693 during the late Devonian (e.g., Grønlie and Roberts, 1989). Thus, the inception of activity along
694 the ENE-WSW trending faults is likely older than the obtained K-Ar ages of the studied gouges,
695 and may have started already in the Devonian (Doré et al., 1999; Kendrick et al., 2004; Faleide et
696 al., 2008; Gernigon et al., 2020).

697 ***5.3.3 WNW-ESE and E-W Striking Faults***

698 As shown by the remote sensing analysis, WNW-ESE and E-W striking lineaments show mutual
699 crosscutting relationship with the other trends (Fig. 3). In the field, WNW-ESE trending faults
700 record dip-slip or strike-slip kinematics. The WNW-ESE and E-W striking faults are mainly
701 associated with iron oxide mineralizations, incohesive brittle fault rocks, quartz, and calcite
702 mineral coatings.

703 Three faults belonging to this lineament set have been dated (Fig. 11). Samples 19.006B and
704 19.078 were taken from two low angle dip-slip faults. These faults are situated in the northern-

and southernmost studied segments of the MNPM where they cut across a granite (19.006B) and a gabbro (19.078). From a structural point of view, these faults are compatible with a compressional stress regime (NW-SE oriented σ_1, Fig. 1a). This compressional stress field may represent the stress field during the Caledonian orogeny. However, E-W and NW-SE thrusts and folds reported by previous authors in the Sunnfjord region and on Hitra and Frøya have been associated with a N-S shortening related to a contractional/transpressional event in the Late Devonian-Early Carboniferous, referred to as the "Solundian phase" (Braathen, 1999; Osmundsen and Andersen, 2001; Sturt and Braathen, 2001). It cannot be excluded that this set of faults originated during the Solundian phase.

K-Ar data of the samples 19.006B and 19.078 indicate that these two faults record a Carboniferous thermal/faulting event, c. 320 Ma ago, and later reactivation during Triassic-Jurassic rifting in an overall E-W extensional regime (Fig. 11). Therefore, they probably experienced a compressional event (the Caledonian or the Solundian phase) and were later reactivated in an extensional manner during Carboniferous and Triassic-Jurassic rifting.

Fault gouge 19.016 was collected from a moderately dipping normal fault. It records a different, younger brittle history which documents an Early Cretaceous origin and bears testimony of a Late Cretaceous reactivation (<97 Ma, Fig. 11) during a NW-SE extensional phase.

5.4 Regional Implications

The mapping, characterization and dating of the brittle structural framework along the MNPM allows us to place new temporal constraints onto the evolution of the margin, as summarized in Figure 12. This figure shows the obtained inverted paleostress fields through time and the strike of the brittle structures that accommodated faulting during the constrained deformation phases.

Out of the many structures preserved along the MNPM, some sets of faults in the Smøla-Hitra batholith may represent the brittle expression of Caledonian deformation. These sets of faults (Fig. 8a-b) show similar orientations and kinematics as along the North Sea Margin, where $^{39}Ar/^{40}Ar$ ages of ca. 450 and 435 Ma were obtained from synkinematic micas (Scheiber et al., 2016). In fact, paleostress inversion of our fault sets resulted in a pure compressional stress regime with σ_1 oriented NW-SE and a transpressional stress regime (R':1.98) with σ_1 oriented NW-SE, both of which are compatible with the Caledonian tectonic stresses reconstructed by other studies (e.g., Séranne, 1992; Scheiber and Viola, 2018; Fig. 12). Another possible interpretation (not illustrated in Fig. 12) is that the compressional stress regime could be related to the Late Devonian-Early Carboniferous N-S-oriented contractional/transpressional Solundian phase, which generated the E-W-trending folds and thrusts in the Solund Basin (North Sea) and on Hitra and Frøya (Braathen, 1999; Osmundsen and Andersen, 2001; Sturt and Braathen, 2001). The same compressional structures on Hitra and Frøya have been also previously interpreted as due to Early Devonian transtensional activity of the MTFC, which would have caused local NW-SE compression, coeval to slightly younger than the emplacement of the Smøla-Hitra batholith (e.g., Krabbendam and Dewey, 1998).

In the area, the MTFC was possibly active in pre-Devonian times accommodating dextral transpression (Séranne, 1992) with the formation of pervasive ductile fabrics that were reactivated during the formation of the MNPM. The MNPM accommodated an extensional history that started in the Early Devonian with the collapse of the Scandinavian Caledonides (Doré et al., 1999; Faleide et al., 2008; Gernigon et al., 2020). A few structural observations onshore East Greenland support the idea that the first rifting phase affecting the NE Atlantic was in the mid-Carboniferous, but this model remains poorly constrained in the MNPM (e.g.,

Stemmerik et al., 2000; Rotevatn et al., 2018). However, our K-Ar ages from NE-SW and NW-SE striking faults support rift initiation along the MNPM in the Carboniferous. This is also in agreement with the dating of Late Carboniferous-Early Permian pseudotachylytes from the Hitra-Snåsa Fault (Sherlock et al., 2004) and of Late Carboniferous cataclasites along the Høybakken Detachment (Kendrick et al., 2004). It can be argued that this Carboniferous event is responsible for the formation of sedimentary basins in the proximal offshore domain of the MNPM, now possibly ascribed to the Late Paleozoic-Early Mesozoic (Osmundsen et al., 2021). More evidence of the Late Carboniferous faulting along the MNPM may have been partly or fully obliterated by later slip deformation and the reworking of originally Carboniferous faults (Fossen et al., 2021). The main rifting phases experienced by the MNPM recorded in the offshore domain are reported in the Permo-Triassic and in the Late Jurassic-Cretaceous (Gernigon et al., 2020). Our data, however, clearly indicate that faulting took place already in the Late Triassic-Early Jurassic and in two pulses during the Cretaceous (Figs. 10, 11, 12). These rifting phases are well documented in the North Sea margin by a rapidly growing database of absolute K-Ar deformation ages (Ksienzyk et al. 2016; Viola et al. 2016; Scheiber and Viola, 2018; Scheiber et al. 2019; Fossen et al., 2021). According to our new dataset, the onshore MNPM recorded the effects of two slightly younger rifting phases in comparison to the rifting phases established in the North Sea margin which may be a result of the northward propagation of rifting (Ren et al., 2003; Gernigon et al., 2020; Zastrozhnov et al., 2020).

During the Triassic-Jurassic faulting event recorded by the onshore MNPM, E-W crustal stretching occurred, as well documented by previous studies from the North Sea and the MNPM (Gómez et al., 2004; Scheiber and Viola, 2018; Gernigon et al., 2020). This rifting phase reactivated older structures and formed epidote-rich cataclasites and quartz veins associated with

NE-SW, NW-SE, and ENE-WSW-striking faults (Figs. 11, 12). Coeval alteration/deep weathering occurred, likely due to fluid circulation along brittle structures dissecting tilted blocks during rifting (e.g., Fredin et al., 2017).

The Cretaceous events along the MNPM have played a key role in the reactivation of older fault zones, forming extensive low temperature mineralizations along the exploited fault planes, such as calcite, prehnite and zeolite. The Early Cretaceous event recorded onshore correlates well with the formation of the offshore Møre and Vøring sedimentary basins and the activity of offshore major boundary faults (Osmundsen and Péron-Pinvidic, 2018; Zastrozhnov et al., 2018, 2020). The Late Cretaceous faulting event could also reflect the reactivation of suitably oriented faults during later stages of rifting prior to the final breakup of the NE Atlantic Ocean (Gernigon et al., 2020). Although similar ages have been reported from onshore faults along the North Sea Margin (Tartaglia et al., 2020; Fossen et al., 2021 and references therein), the Late Cretaceous faulting activity in the MNPM is only documented in the distal offshore domain (e.g., Péron-Pinvidic et al., 2013; Gernigon et al., 2020).

In the offshore domain, the MTFC separates the Jurassic–Cretaceous North Sea basins from the Cretaceous basins of the MNPM (Redfield et al., 2005), suggesting important offshore Cretaceous activity (Péron-Pinvidic et al., 2013). The faults parallel to the onshore MTFC recorded the rifting events from the Early Jurassic to the Late Cretaceous, supporting the active tectonic role of the multiply reactivated MTFC during rifting and the development of the margin.

6. CONCLUSIONS

The MNPM derives from a complex polyphase faulting history. Its evolution was influenced by the effects of the spatial orientation of old, inherited structures, such as the Caledonian orogen-parallel structural grain and the MTFC (*cf.* Osmundsen et al., 2006; Phillips et al., 2019; Schiffer et al., 2019). By means of remote sensing lineament analysis, field work, microstructural analysis, paleostress inversion, mineralogical characterization and K-Ar dating of illite separated from selected fault zones, six tectonic events have been identified. From older to younger these are (Fig. 12):

i) Paleozoic NE-SW compression forming WNW-ESE-trending and N(NE)-dipping low-angle thrust faults;

ii) Paleozoic transpression with σ_1 oriented NW-SE forming conjugate NW-SE sinistral and E-W dextral strike slip faults;

iii) A Carboniferous faulting event associated with rift initiation forming NW-SE and NE-SW, variably dipping, faults.

iv) Late Triassic-Early Jurassic E-W extension at c. 202 and 177 Ma forming epidote and quartz-coated, N-S striking, generally normal faults, and coeval alteration of the host rock due to faulting-enhanced fluid circulation;

v) Early Cretaceous NW-SE extension representing the second rifting stage documented from the offshore domain of the MNPM, leading to the formation of normal, transtensional NE-SW and N-S striking faults;

vi) Late Cretaceous (K-Ar ages of c. 71, 80, 86, 91 Ma) extension reactivating suitably oriented pre-existing faults, with extensive synkinematic precipitation of low temperature coatings (prehnite, zeolite).

The lack of a preserved sedimentary cover and the long brittle evolution of the MNPM make the reconstruction of the tectonic evolution of the margin challenging. However, our new radiometric ages fill in the gap of absolute dating of fault activity along the MNPM.

Fault dating coupled with multiscalar structural analysis has been shown to be key to the study of the polyphase history of the margin. Finally, the applied workflow may assist the interpretation of the structural framework of the offshore domain, leading to high-resolution structural models and better exploration predictive tools.

Table and Figure Captions

Table 1- *Field data of sampled and dated fault zones grouped into three sets according to their strike (WNW-ESE, ENE-WNW, NE-SW). (N: Normal fault, R: Reverse fault; S: Sinistral fault; X: Unknown sense of slip)*

Table 2- *XRD data of the dated samples separated in five grain size fractions (<0.1, 0.1-0.4, 0.4-2, 2-6 and 6-10 μm). (Qtz: quartz, Kfs: K-feldspar, Plg: plagioclase; Cc: calcite, Ep: epidote; Amp: amphibole; Px: pyroxene; Ill: illite; Ms: muscovite; Palyg: palygorskite; Kln:*

kaolinite; Chl: chlorite; Sm: smectite; Verm: vermiculite; Lepid: lepidocrocite; Zeo: zeolite; Stb: stilbite; Ap: apatite; Anl: analcime; GOF: Goodness of Fit).

Table 3 - *K-Ar data of 12 fault gouge and 1 altered rock (19.042E) samples.*

Figure 1 - *Simplified geological map of the on- and offshore mid-Norwegian Passive Margin. Drawn after Faleide et al. (2008) and Slagstad et al. (2011). (MTFC: Møre-Trøndelag Fault Complex; WGR: Western Gneiss Region).*

Figure 2 - *Map showing hillshaded LiDAR DEMs and bedrock lineaments from the coastal MNPM color-coded according to their strike (as shown in the associated rose diagrams). (a) Lineaments from the entire MNPN, mapped at the 1:100.000 scale. (b) Lineaments from the northern MNPM (Hitra, Frøya and Smøla), mapped at the 1:10.000 scale, (c) Lineaments from the southern segment of the MNPM, mapped at the 1:10.000 scale.*

Figure 3 – *Maps showing examples of manually mapped lineaments at two different scales on (a) northeastern Hitra and (b) western Smøla. The black circles highlight mapped crosscutting relationships between variably oriented lineaments.*

Figure 4 - *(a) Map of the investigated structural sites. Dark grey dots indicate the location of the dated fault gouge samples (Table 1); (b) Rose diagrams showing the strike orientation of fault and fracture zones, sorted according to the main decorating mineral phase.*

Figure 5 *- Photographs of representative fault zones. (a) ENE-WSW outcrop of a strand of the MTFC (Jøsnøya, Hitra island); (b) same outcrop as in (a), this strand of the MTFC is cut by high-angle normal faults, oriented NNW-SSE; (c) c. 10 m thick fault zone, with the principal slip surface oriented 322/76 and a (d) fault core containing cataclasite and gouge (Hitra island); (e) E-dipping fault plane with a 10 cm-thick core containing fine-grained quartz and epidote cut by milky white prehnite veins (pointed out by yellow arrows, Hitra island); (f) NE-SW transtensional fault plane with calcite and zeolite coating (Runde island).*

Figure 6 *– Sampled and dated fault zones divided into three sets according to their strike: WNW–ESE and E-W (a - c); ENE – WSW (d – –); –NE-SSW (j - m). Red lines highlight principal slip* surfaces, and the yellow squares indicate the sampled area. More details in the text and Table 1.

Figure 7 - Microphotographs of representative fault rocks from Hitra island. (a) Granitic protocataclasite characterized by pervasive fracturing and epidote mineralization. The host rock is partially altered, as indicated by the occurrence of chlorite (Chl) and saussurritic plagioclase (Plg). Several generations of progressively finer-grained epidote mineralizations can be

identified (Ep_1, Ep_2, Ep_3). (b) Quartz (Qtz)-rich cataclasite containing a clast of fine-grained epidote-bearing cataclasite (Ep_3). The quartz-rich layer contains a younger quartz vein (Qtz_2) localized at the contact between an epidote-bearing cataclastic layer (top) and the quartz-rich cataclasite (bottom, Qtz_1). Note the occurrence of multiple layers of variably sized epidote cataclasites (Ep_2, Ep_1). (c) Prehnite (Prh) vein and cataclastic layer (top) cutting across an older quartz-epidote-bearing cataclasite. This cataclasite contains clasts of epidote-bearing layers embedded in a coarse-grained, quartz-rich vein/cataclastic layer. (d) Prehnite vein disrupting the layered structure of older epidote- and quartz-bearing cataclasite. (e) Fine-grained, cataclasite containing coarse grained clasts of epidote-, quartz and prehnite-bearing cataclasite embedded in a fine-grained matrix. (f) Calcite (Cc) vein associated with euhedral zeolite crystals. (a, c-e) Sample 19’009A, N 63°’1.079' E 08°48.838'; (b) Sample 1’.002B, N 63°’8.868' E 08°47.255'; (f) Sample ’9.006, N 63°’8.339' E 08°40.505'.

Figure 8 - *Paleostress tensors computed from the inversion of fault-slip data from the onshore MNPM: stereonets (a) to (e) are tentatively sorted from oldest to youngest (see text for explanation). Stereoplots are Schmidt, lower hemisphere projections. (bfr: brittle fault rocks; Ep: epidote; Chl: chlorite; Qz: quartz: Prh: Prehnite; Cc: Calcite).*

Figure 9 - *Pie charts of mineral concentrations [wt%] derived from XRD of each of the dated fractions of three representative fault gouges of different ages (i.e., ages of the finest grain size fractions): 19.070 (80 ± 1 Ma), 19.042A (86 ± 1 Ma), 19.006B (197 ± 3 Ma).*

Figure 10 - K-Ar age vs. grain size fraction diagram. Each point in the diagram represents the age of a specific grain size fraction. The gray bars indicate deduced tectonic events and are also reported in Figs. 11 and 12.

Figure 11 - *Radial diagram of fault gouge and altered rock K-Ar ages plotted as a function of the fault plane orientation. (G.s.f.: grain size fraction). Only K-Ar ages interpreted as geologically meaningful (cf. text and figure 10) are shown.*

Figure 12 - *Schematic summary of the obtained paleostress fields through time and strike of active brittle structures. The stereoplots represent the inverted paleostress regimes in present-day coordinates. The white, grey, and black arrows in the stereoplots represent the orientation of* σ_1, σ_2 *and* σ_3, *respectively.*

ACKNOWLEDGMENTS

Our research work was funded by the BASE 2 project ("Basement fracturing and weathering onshore and offshore Norway—Genesis, age, and landscape development" – Part 2), a research initiative launched and steered by the Geological Survey of Norway and supported by Equinor ASA, Aker BP ASA, Lundin Energy Norway AS, Spirit Energy Norway AS, Wintershall Dea Norge, and NGU. We thank all BASE colleagues for continuous discussion and constructive

912 inputs. Ruikai Xie from NGU laboratories is thanked for careful K analysis. The high-resolution
913 LiDAR-based elevation model used in this study was made available from the Statens Kartverk
914 to the NGU through the Geonorge portal of spatial data. Alvar Braathen, Per Terje Osmundsen
915 and Enrico Tavarnelli are thanked for their insightful and constructive inputs and comments.

916

917 REFERENCES CITED

918 Angelier, J., 1984, Tectonic analysis of fault slip data sets: Journal of Geophysical Research:
919 Solid Earth, v. 89, no. B7, p. 5835-5848, doi:10.1029/jb089ib07p05835

920 Blystad, P., 1995, Structural elements of the Norwegian continental shelf. Part 2: The Norwegian
921 Sea region: NPD Bulletin, v. 8

922 Bott, M. H. P., 1959, The mechanics of oblique slip faulting: Geological magazine, v. 96, no. 2,
923 p. 109-117

924 Braathen, A., 1999, Kinematics of post-Caledonian polyphase brittle faulting in the Sunnfjord
925 region, western Norway, Tectonophysics, v. 302(1–2), p. 99-121, doi:10.1016/S0040-
926 1951(98)00281-9.

927 Braathen, A., Osmundsen, P.T., Nordgulen, 0., Roberts, D., Meyer, G.B., 2002, Orogen-parallel
928 extension of the Caledonides in northern Central Norway: an overview: Norsk Geologisk
929 Tidsskrift, v. 82, pp. 225–241

930 Braathen, A., Osmundsen, P. T., and Gabrielsen, R. H., 2004, Dynamic development of fault
931 rocks in a crustal-scale detachment: An example from western Norway: Tectonics, v. 23,
932 no. 4, p. 21, doi:10.1029/2003tc001558

933 Breivik, A. J., Mjelde, R., Raum, T., Faleide, J. I., Murai, Y., and Flueh, E. R., 2011, Crustal
934 structure beneath the Trøndelag Platform and adjacent areas of the mid-Norwegian
935 margin, as derived from wide-angle seismic and potential field data: Norwegian Journal
936 of Geology, v. 90, p. 141-161

937 Bungum, H., Alsaker, A., Kvamme, L., and Hansen, R., 1991, Seismicity and seismotectonics of
938 Norway and nearby continental shelf areas: Journal of Geophysical Research: Solid
939 Earth, v. 96, no. B2, p. 2249-2265, doi:10.1029/90JB02010

940 Ceccato, A., Viola, G., Tartaglia, G., and Antonellini, M., 2021a, *In–situ* quantification of
941 mechanical and permeability properties on outcrop analogues of offshore fractured and
942 weathered crystalline basement: Examples from the Rolvsnes granodiorite, Bømlo,
943 Norway: Marine and Petroleum Geology, v. 124, doi:10.1016/j.marpetgeo.2020.104859

944 Ceccato, A., Viola G., Antonellini, M., Tartaglia, G., Ryan, E. J., 2021b, Constraints upon fault
945 zone properties by combined structural analysis of virtual outcrop models and discrete
946 fracture network modelling. Journal of Structural Geology, 152(September), 104444,
947 doi:10.1016/j.jsg.2021.104444

948 Corfu, F., Andersen, T. B., and Gasser, D., 2014, The Scandinavian Caledonides: main features,
949 conceptual advances and critical questions: Geol. Soc. London, Spec. Publ., v. 390, no. 1,
950 p. 9-43, doi:10.1144/sp390.25

951 Davids, K., Wemmer, K., Zwingmann, H., Kohlmann, F., Jacobs, J., and Bergh, S. G., 2013, K–
952 Ar illite and apatite fission track constraints on brittle faulting and the evolution of the
953 northern Norwegian passive margin: Tectonophysics, v. 608, p. 196-
954 211,doi:10.1016/j.tecto.2013.09.035

955 Delvaux, D., and Sperner, B., 2003, Stress tensor inversion from fault kinematic indicators and
956 focal mechanism data: the TENSOR program.: Geol. Soc. London, Spec. Publ., v. 212, p.
957 75-100, doi:10.1144/GSL.SP.2003.212.01.06

958 Doré, A., Lundin, E., Fichler, C., and Olesen, O., 1997, Patterns of basement structure and
959 reactivation along the NE Atlantic margin: Journal of the Geological Society, v. 154, no.
960 1, p. 85-92, doi:10.1144/gsjgs.154.1.0085

961 Doré, A., Lundin, E., Jensen, L., Birkeland, Ø., Eliassen, P., and Fichler, C., Principal tectonic
962 events in the evolution of the northwest European Atlantic margin, *in* Proceedings
963 Geological society, London, petroleum geology conference series1999, Volume 5,
964 Geological Society of London, p. 41-61

965 Doré, A. G., Lundin, E. R., Kusznir, N. J., and Pascal, C., 2008, Potential mechanisms for the
966 genesis of Cenozoic domal structures on the NE Atlantic margin: pros, cons and some
967 new ideas: Geological Society, London, Special Publications, v. 306, no. 1, p. 1-26,
968 doi:10.1144/sp306.1

969 Duffy, O. B., Bell, R. E., Jackson, C. A. L., Gawthorpe, R. L., and Whipp, P. S., 2015, Fault
970 growth and interactions in a multiphase rift fault network: Horda Platform, Norwegian
971 North Sea: Journal of Structural Geology, v. 80, p. 99-119, doi:10.1016/j.jsg.2015.08.015

Faleide, J. I., Tsikalas, F., Breivik, A. J., Mjelde, R., Ritzmann, O., Engen, Ø., Wilson, J., and Eldholm, O., 2008, Structure and evolution of the continental margin off Norway and the Barents Sea: Episodes, v. 31, no. 1, p. 82-91, doi:10.18814/epiiugs/2008/v31i1/012

Fazlikhani, H., Aagotnes, S. S., Refvem, M. A., Hamilton-wright, J., Bell, R., Fossen, H., Gawthorpe, R., Jackson, C. A.-L., and Rotevatn, A., 2020, Strain migration during multiphase extension, Stord Basin, northern North Sea rift, v. 33, no. 2, p. 1474-1496, doi:10.31223/osf.io/b8acf

Fjellanger, E., Surlyk, F., Wamsteeker, L. C., & Midtun, T., 2005, Upper Cretaceous basin-floor fans in the Vøring Basin, Mid Norway shelf. In B. Wandaas, et al. (Eds.), Onshore-Offshore Relationships on the North Atlantic Margin, Special Publications, v. 12, pp. 135–164. Trondheim, Norway: Norwegian Petroleum Society, doi:10.1016/S0928-8937(05)80047-5

Fossen, H., 2010, Extensional tectonics in the North Atlantic Caledonides: a regional view: Geol. Soc. London, Spec. Publ. v. 335, doi:10.1144/SP335.31 0305-8719

Fossen, H., Ksienzyk, A. K., Rotevatn, A., Bauck, M. S., and Wemmer, K., 2021, From widespread faulting to localised rifting: Evidence from K-Ar fault gouge dates from the Norwegian North Sea rift shoulder: Basin Research. v. 33, p. 1934–1953, doi:10.1111/bre.12541

Fredin, O., Viola, G., Zwingmann, H., Sorlie, R., Bronner, M., Lie, J. E., Grandal, E. M., Muller, A., Margreth, A., Vogt, C., and Knies, J., 2017, The inheritance of a Mesozoic landscape in western Scandinavia: Nat. Commun., v. 8, p. 14879, doi:10.1038/ncomms14879

Gabrielsen, R., Færseth, R., 1988, Cretaceous and Tertiary reactivation of master fault zones of the Barents Sea, *in* Proceedings Tertiary Tectonics of Svalbard. Extended Abstracts from Symposium Held in Oslo. Norwegian Polar Institute Report Series v. 46, p. 93-97.

Gabrielsen, R. H., and Braathen, A., 2014, Models of fracture lineaments - Joint swarms, fracture corridors and faults in crystalline rocks, and their genetic relations: Tectonophysics, v. 628, p. 26-44, doi:10.1016/j.tecto.2014.04.022

Gabrielsen, R. H., Braathen, A., Dehls, J., and Roberts, D., 2002, Tectonic lineaments of Norway: Norw. J. Geol., v. 82, p. 153-174

Gabrielsen, R. H., Nystuen, J. P., and Olesen, O., 2018, Fault distribution in the Precambrian basement of South Norway: Journal of Structural Geology, v. 108, p. 269-289, doi:10.1016/j.jsg.2017.06.006

Gabrielsen, R. H., Odinsen, T., and Grunnaleite, I., 1999, Structuring of the Northern Viking Graben and the More Basin; the influence of basement structural grain and the particular role of the More Trondelag Fault Complex: Marine and Petroleum Geology, v. 16, p. 443-465

Gautneb, H., and Roberts, D., 1989, Geology and petrochemistry of the Smela-Hitra Batholith, Central Norway: Nor. geol. unders. Bull., v. 416, p. 1-24

Gernigon, L., Franke, D., Geoffroy, L., Schiffer, C., Foulger, G. R., and Stoker, M., 2020, Crustal fragmentation, magmatism, and the diachronous opening of the Norwegian-Greenland Sea: Earth-Science Reviews, v. 206, doi:10.1016/j.earscirev.2019.04.011

Gómez, M., Vergés, J., Fernàndez, M., Torne, M., Ayala, C., Wheeler, W., and Karpuz, R., 2004, Extensional geometry of the Mid Norwegian Margin before Early Tertiary continental breakup: Marine and Petroleum Geology, v. 21, no. 2, p. 177-194, doi:10.1016/j.marpetgeo.2003.11.017

Grønlie, A., and Roberts, D., 1989, Resurgent strike-slip duplex development along the Hitra-Snåsa and Verran faults, Møre-Trøndelag fault zone, central Norway: Journal of structural geology, v. 11, no. 3, p. 295-305

Grønlie, A., Roberts, D., and Nilsen, B., 1991, Brittle deformation history of fault rocks on the Fosen Peninsula, Trøndelag, Central Norway, NGU Bulletin, v. 421.

Hancock, P. L., 1985, Brittle microtectonics: principles and practice. Journal of structural geology, 7(3-4), 437-457.

Kendrick, M. A., Eide, E. A., Roberts, D., and Osmundsen, P. T., 2004, The Middle to Late Devonian Høybakken detachment, central Norway: ^{40}Ar–^{39}Ar evidence for prolonged late/post-Scandian extension and uplift: Geological Magazine, v. 141, no. 3, p. 329-344, doi:10.1017/s0016756803008811

Krabbendam, M., and Dewey, J. F. ,1998, Exhumation of UHP rocks by transtension in the Western Gneiss Region, Scandinavian Caledonides. Geological Society, London, Special Publications, v. 135, no. 1, p. 159–181, doi:10.1144/gsl.sp.1998.135.01.

Krabbendam, M., Wain, A., and Andersen, T. B., 2000, Pre-Caledonian granulite and gabbro enclaves in the Western Gneiss Region, Norway: indications of incomplete transition at high pressure: Geological Magazine, v. 137, p. 235–255

1034 Ksienzyk, A. K., Wemmer, K., Jacobs, J., Fossen, H., Schomberg, A. C., Süssenberger, A.,
1035 Lünsdorf, N. K., and Bastesen, E., 2016, Post-Caledonian brittle deformation in the
1036 Bergen area: Norw. J. Geol., v. 96, no. 3, doi:10.17850/njg96-3-06

1037 Lacombe, O., 2012, Do fault slip data inversions actually yield "paleostress" that can be
1038 compared with contemporary stresses? A critical discussion: Comptes Rendus
1039 Geoscience, v. 344, p. 159-173, doi: 10.1016/j.crte.2012.01.006

1040 Lacombe, O., Jolivet, L., Le Pourhiet, L., Lecomte, E., and Mehl, C., 2013, Initiation, geometry
1041 and mechanics of brittle faulting in exhuming metamorphic rocks: insights from the
1042 northern Cycladic islands (Aegean, Greece): Bull. Soc. géol. France, v. 184, no. 4-5, p.
1043 383-403, doi: 10.2113/gssgfbull.184.4-5.383

1044 Lundin, E., and Doré, A., 2002, Mid-Cenozoic post-breakup deformation in the 'passive'margins
1045 bordering the Norwegian–Greenland Sea: Marine and Petroleum Geology, v. 19, no. 1, p.
1046 79-93

1047 Lundin, E. R., and Doré, A. G., 2011, Hyperextension, serpentinization, and weakening: A new
1048 paradigm for rifted margin compressional deformation: Geology, v. 39, no. 4, p. 347-350.
1049 doi:10.1130/G31499.1

1050 Malatesta, C., Crispini, L., Ildefonse, B., Federico, L., Lisker, F., and Läufer, A., 2021,
1051 Microstructures of epidote-prehnite bearing damaged granitoids (northern Victoria Land,
1052 Antarctica): clues for the interaction between faulting and hydrothermal fluids. Journal of
1053 Structural Geology,147, 104350, doi:10.1016/j.jsg.2021.104350

Mattila, J., and Viola, G., 2014, New constraints on 1.7 Gyr of brittle tectonic evolution in southwestern Finland derived from a structural study at the site of a potential nuclear waste repository (Olkiluoto Island): J. Struct. Geol., v. 67, p. 50-74, doi:10.1016/j.jsg.2014.07.003

Munro, M. A., and Blenkinsop, T. G., 2012, MARD—A moving average rose diagram application for the geosciences: Computers & Geosciences, v. 49, p. 112-120, doi:10.1016/j.cageo.2012.07.012

Nasuti, A., Pascal, C., and Ebbing, J., 2012, Onshore–offshore potential field analysis of the Møre–Trøndelag Fault Complex and adjacent structures of Mid Norway: Tectonophysics, v. 518-521, p. 17-28, doi:10.1016/j.tecto.2011.11.003

Nasuti, A., Pascal, C., Ebbing, J., and Tønnesen, J. F., 2011, Geophysical characterisation of two segments of the Møre-Trøndelag Fault Complex, Mid Norway: Solid Earth, v. 2, no. 2, p. 125-134, doi:10.5194/se-2-125-2011

Nordbäck, N., Mattila, J., Zwingmann, H., and Viola, G., 2022, Precambrian fault reactivation revealed by structural and K-Ar geochronological data from the spent nuclear fuel repository in Olkiluoto, southwestern Finland: Tectonophysics, 824, pp. 1 – 22, doi:10.1016/j.tecto.2022.229208

Osmundsen, P. T., and Andersen, T. B. 2001, The middle Devonian basins of western Norway: sedimentary response to large-scale transtensional tectonics?. Tectonophysics, 332(1-2), 51-68. doi:10.1016/S0040-1951(00)00249-3

Osmundsen, P.T., Braathen, A., Sommaruga, A., Skilbrei, J.R., Nordgulen, Ø., Roberts, D., Andersen, T.B., Olesen, O., Mosar, J., 2005. Metamorphic core complexes and gneiss-cored culminations along the Mid-Norwegian margin: and overview and some current ideas. In: Wandås (Ed.), Onshore-Offshore Relationships on the North Atlantic Margin. Norwegian Petroleum Society (NPF) Special Publication, 12, pp. 29–41

Osmundsen, P. T., Eide, A. E., Haabesland, N. E., Roberts, D., Andersen, T. B., Kendrick, M., Bingen, B., Braathen, A., and Redfield, T. F., 2006, Kinematics of the Høybakken detachment zone and the Møre–Trøndelag Fault Complex, central Norway: J. Geol. Soc. London, v. 163, p. 303-318, doi:10.1144/0016-764904-129

Osmundsen, P. T., and Péron-Pinvidic, G., 2018, Crustal-scale fault interaction at rifted margins and the formation of domain-bounding breakaway complexes: Insights from offshore Norway. Tectonics, 37, p. 935–964, doi:10.1002/2017TC004792

Osmundsen, P. T., Péron-Pinvidic, G., and Bunkholt, H., 2021, Rifting of collapsed orogens: successive incision of continental crust in the proximal margin offshore Norway. Tectonics, 40(2), e2020TC006283, doi:10.1029/2020tc006283

Péron-Pinvidic, G., G. Manatschal, and P. T. Osmundsen, 2013, Structural comparison of archetypal Atlantic rifted margins: A review ofobservations and concepts, Marine and Petroleum Geology, 43,21–47, doi: 10.1016/j.marpetgeo.2013.02.002

Péron-Pinvidic, G., and Osmundsen, P. T., 2020, From orogeny to rifting: insights from the Norwegian 'reactivation phase': Sci Rep, v. 10, no. 1, p. 14860, doi:10.1038/s41598-020-71893-z

1095 Péron-Pinvidic, G., Osmundsen, P. T., and Bunkholt, H., 2020, The proximal domain of the Mid-
1096 Norwegian rifted margin: The Trøndelag Platform revisited: Tectonophysics, v. 790,
1097 doi:10.1016/j.tecto.2020.228551

1098 Petford, N., and McCaffrey, K., 2003, Hydrocarbons in crystalline rocks: an introduction:
1099 Geological Society, London, Special Publications, v. 214, no. 1, p. 1-5,
1100 doi:10.1144/gsl.Sp.2003.214.01.01

1101 Petit, J. P., 1987, Criteria for the sense of movement on fault surfaces in brittle rocks. Journal of
1102 structural Geology, 9(5-6), 597-608.

1103 Phillips, T. B., Fazlikhani, H., Gawthorpe, R. L., Fossen, H., Jackson, C. A. L., Bell, R. E.,
1104 Faleide, J. I., and Rotevatn, A., 2019, The influence of structural inheritance and
1105 multiphase extension on rift development, the northern North Sea: Tectonics, v. 38, no.
1106 12, p. 4099-4126, doi:10.1029/2019tc005756

1107 Pollard, D. D., 2000, Strain and stress: Discussion: Journal of Structural Geology, v. 22, p. 1359-
1108 1367

1109 Redfield, T. F., Braathen, A., Gabrielsen, R. H., Osmundsen, P. T., Torsvik, T. H., and
1110 Andriessen, P. A. M., 2005, Late Mesozoic to Early Cenozoic components of vertical
1111 separation across the Møre–Trøndelag Fault complex, Norway: Tectonophysics, v. 395,
1112 no. 3-4, p. 233-249, doi:10.1016/j.tecto.2004.09.012

1113 Redfield, T. F., and Osmundsen, P. T., 2009, The Tjellefonna fault system of Western Norway:
1114 Linking late-Caledonian extension, post-Caledonian normal faulting, and Tertiary rock

column uplift with the landslide-generated tsunami event of 1756: Tectonophysics, v. 474, no. 1-2, p. 106-123, doi:10.1016/j.tecto.2009.02.006

Redfield, T. F., Torsvik, T. H., Andriessen, P. A. M., and Gabrielsen, R. H., 2004, Mesozoic and Cenozoic tectonics of the Møre Trøndelag Fault Complex, central Norway: constraints from new apatite fission track data: Physics and Chemistry of the Earth, Parts A/B/C, v. 29, no. 10, p. 673-682, doi:10.1016/j.pce.2004.03.005

Ren, S., Faleide, J. I., Eldholm, O., Skogseid, J., and Gradstein, F., 2003, Late Cretaceous–Paleocene tectonic development of the NW Vøring Basin: Marine and Petroleum Geology, v. 20, no. 2, p. 177-206, doi:10.1016/s0264-8172(03)00005-9

Reston, T. J., 2005, Polyphase faulting during the development of the west Galicia rifted margin: Earth and Planetary Science Letters, v. 237, no. 3-4, p. 561-576, doi:10.1016/j.epsl.2005.06.019

Riber, L., Dypvik, H., and Sørlie, R., 2015, Altered basement rocks on the Utsira High and its surroundings, Norwegian North Sea: Norw. J. Geol, doi:10.17850/njg95-1-04

Riber, L., Dypvik, H., Sorlie, R., Aal-E-Muhammad Naqvi, S. A., Stangvik, K., Oberhardt, N., and Schroeder, P. A., 2017, Comparison of deeply buried paleoregolith profiles, Norwegian North Sea, with outcrops from southern Sweden and Georgia, USA — Implications for petroleum exploration: Palaeogeogr. Palaeocl., v. 471, p. 82-95, doi:10.1016/j.palaeo.2017.01.043

Rotevatn, A., Kristensen, T. B., Ksienzyk, A. K., Wemmer, K., Henstra, G. A., Midtkandal, I., et al., 2018, Structural Inheritance and Rapid Rift-Length Establishment in a Multiphase

Rift: The East Greenland Rift System and its Caledonian Orogenic Ancestry. Tectonics, 37, 1858–1875, doi:10.1029/2018TC005018

Saintot, A., Stephens, M. B., Viola, G., and Nordgulen, Ø., 2011, Brittle tectonic evolution and paleostress field reconstruction in the southwestern part of the Fennoscandian Shield, Forsmark, Sweden: Tectonics, v. 30, no. 4, doi:10.1029/2010tc002781

Scheiber, T., Fredin, O., Viola, G., Jarna, A., Gasser, D., and Łapińska-Viola, R., 2015, Manual extraction of bedrock lineaments from high-resolution LiDAR data: methodological bias and human perception: Gff, v. 137, no. 4, p. 362-372, doi:10.1080/11035897.2015.1085434

Scheiber, T., Viola, G., Wilkinson, C.M., Ganerød, M., Skår, O. and Gasser D., 2016, Direct $^{40}Ar/^{39}Ar$ dating of Late-Ordovician and Silurian brittle faulting in the southwestern Norwegian Caledonides. Terra Nova 28, 374-382, doi:10.1111/ter.12230

Scheiber, T., and Viola, G., 2018, Complex Bedrock Fracture Patterns: A Multipronged Approach to Resolve Their Evolution in Space and Time: Tectonics, v. 37, no. 4, p. 1030-1062, doi:10.1002/2017tc004763

Scheiber, T., Viola, G., van der Lelij, R., Margreth, A., and Schönenberger, J., 2019, Microstructurally-constrained versus bulk fault gouge K-Ar dating: J. Struct. Geol., v. 127, doi:10.1016/j.jsg.2019.103868

Schiffer, C., Doré, A. G., Foulger, G. R., Franke, D., Geoffroy, L., Gernigon, L., Holdsworth, B., Kusznir, N., Lundin, E., McCaffrey, K. et al., 2019, Structural inheritance in the North Atlantic: Earth-Science Reviews, v. 206, doi:10.1016/j.earscirev.2019.102975

Séranne, M., 1992, Late Palaeozoic kinematics of the Møre-Trøndelag Fault Zone and adjacent areas, central Norway·: Norsk Geologisk Tidsskrift, v. 72, p. 141-158

Sherlock, S. C., Watts, L. M., Holdsworth, R. E., and Roberts, D., 2004, Dating fault reactivation by Ar/Ar laserprobe: an alternative view of apparently cogenetic mylonite–pseudotachylite assemblages: J. Geol. Soc. London, v. 161, no. 3, p. 335-338, doi:10.1144/0016-764903-160

Slagstad, T., Davidsen, B., and Daly, J. S., 2011, Age and composition of crystalline basement rocks on the Norwegian continental margin: offshore extension and continuity of the Caledonian–Appalachian orogenic belt: J. Geol. Soc. London, v. 168, no. 5, p. 1167-1185, doi:10.1144/0016-76492010-136

Sommaruga, A., Bøe, R., 2002. Geometry and subcrop maps of shallow Jurassic basins along the Mid-Norway coast. Marine and Petroleum Geology 19, 1029–1042

Stemmerik, L., Ineson, J. R., and Mitchell, J. G., 2000, Stratigraphy of the Rotliegend Group in the Danish part of the Northern Permian Basin, North Sea: Journal of the Geological Society, London, v. 157, p. 1127–1136

Sturt, B. A., and Braathen, A., 2001, Deformation and metamorphism of Devonian rocks in the outer Solund area, western Norway: implications for models of Devonian deformation. International Journal of Earth Sciences: Geologische Rundschau, 90(2), 270, doi:10.1007/s005310000131

Tanner, D. C., Ziesch, J., and Krawczyk, C. M., 2019, Quantifying the Death of Growth Faults on a Passive Margin - Evidence from 3D Seismics within the Otway Basin, Australia, Volume 2019, p. T33D-0399

Tartaglia, G., 2021, Integrated study of the tectonic evolution of the mid-Norwegian Passive Margin [Ph.D. thesis]: University of Bologna, 197 p.

Tartaglia, G., Viola, G., van der Lelij, R., Scheiber, T., Ceccato, A., and Schönenberger, J., 2020, "Brittle structural facies" analysis: A diagnostic method to unravel and date multiple slip events of long-lived faults: Earth and Planetary Science Letters, v. 545, doi:10.1016/j.epsl.2020.116420

Theissen-Krah, S., Zastrozhnov, D., Abdelmalak, M. M., Schmid, D. W., Faleide, J. I., and Gernigon, L., 2017, Tectonic evolution and extension at the Møre Margin – Offshore mid-Norway: Tectonophysics, v. 721, p. 227-238, doi:10.1016/j.tecto.2017.09.009

Torgersen, E., Viola, G., Zwingmann, H., and Harris, C., 2015, Structural and temporal evolution of a reactivated brittle-ductile fault - Part II: Timing of fault initiation and reactivation by K-Ar dating of synkinematic illite/muscovite: Earth Planet. Sc. Lett., v. 410, p. 212-224, doi:10.1016/j.epsl.2014.11.013

Trice, R., Hiorth, C., and Holdsworth, R., 2019, Fractured basement play development on the UK and Norwegian rifted margins: Geological Society, London, Special Publications, doi:10.1144/sp495-2018-174

Twiss, R. J., and Unruh, J. R., 1998, Analysis of fault slip inversions: Do they constrain stress or strain rate?: J. Geoph. Res., v. 103, p. 12205-12222

van der Pluijm, B. A., Hall, C. M., Vrolijk, P. J., Pevear, D. R., and Covey, M. C., 2001, The dating of shallow faults in the Earth's crust: Nature, v. 412, p. 172-174

Verdel, C., van der Pluijm, B. A., and Niemi, N., 2012, Variation of illite/muscovite $^{40}Ar/^{39}Ar$ age spectra during progressive low-grade metamorphism: an example from the US Cordillera: Contrib. Mineral. Petr., v. 164, no. 3, p. 521-536, doi:10.1007/s00410-012-0751-7

Viola, G., Ganerod, G. V., and Wahlgren, C. H., 2009, Unraveling 1.5 Ga of brittle deformation history in the Laxemar-Simpevarp area, southeast Sweden: A contribution to the Swedish site investigation study for the disposal of highly radioactive nuclear waste: Tectonics, v. 28, doi:10.1029/2009tc002619

Viola, G., Scheiber, T., Fredin, O., Zwingmann, H., Margreth, A., and Knies, J., 2016, Deconvoluting complex structural histories archived in brittle fault zones: Nat. Commun., v. 7, p. 13448, doi:10.1038/ncomms13448

Viola, G., Torgersen, E., Mazzarini, F., Musumeci, G., van der Lelij, R., Schönenberger, J., and Garofalo, P. S., 2018, New Constraints on the Evolution of the Inner Northern Apennines by K-Ar Dating of Late Miocene-Early Pliocene Compression on the Island of Elba, Italy: Tectonics, v. 37, no. 9, p. 3229-3243, doi:10.1029/2018tc005182

Vrolijk, P., Pevear, D., Covey, M., and LaRiviere, A., 2018, Fault gouge dating: history and evolution: Clay Minerals, v. 53, no. 3, p. 305-324./10.1180/clm.2018.22

Wallace, R. E., 1951, Geometry of shearing stress and relation to faulting: The Journal of geology, v. 59, no. 2, p. 118-130

1218 Walsh, E. O., Hacker, B. R., Gans, P. B., Wong, M. S., and Andersen, T. B., 2013, Crustal
1219 exhumation of the Western Gneiss Region UHP terrane, Norway: $^{40}Ar/^{39}Ar$
1220 thermochronology and fault-slip analysis. Tectonophysics, 608, 1159-1179,
1221 doi:10.1016/j.tecto.2013.06.030

1222 Wehrens, P., Berger, A., Peters, M., Spillmann, T., and Herwegh, M., 2016, Deformation at the
1223 frictional-viscous transition: Evidence for cycles of fluid-assisted embrittlement and
1224 ductile deformation in the granitoid crust.Tectonophysics,693, 66-84,
1225 doi:10.1016/j.tecto.2016.10.022

1226 Weisenberger, T., Bucher, K., 2010, Zeolites in fissures of granites and gneisses of the Central
1227 Alps. J. Metamorph. Geol.28, 825–847, doi:10.1111/j.1525-1314.2010.00895.x

1228 Will, T. M., and Frimmel, H. E., 2018, Where does a continent prefer to break up? Some lessons
1229 from the South Atlantic margins: Gondwana Research, v. 53, p. 9-19,
1230 doi:10.1016/j.gr.2017.04.014

1231 Wilson, R. W., McCaffrey, K. J. W., Holdsworth, R. E., Imber, J., Jones, R. R., Welbon, A. I. F.,
1232 and Roberts, D., 2006, Complex fault patterns, transtension and structural segmentation
1233 of the Lofoten Ridge, Norwegian margin: Using digital mapping to link onshore and
1234 offshore geology: Tectonics, v. 25, no. 4, doi:10.1029/2005tc001895

1235 Zastrozhnov, D., Gernigon, L., Gogin, I., Abdelmalak, M. M., Planke, S., Faleide, J. I., Eide, S.,
1236 and Myklebust, R., 2018, Cretaceous-Paleocene Evolution and Crustal Structure of the
1237 Northern Vøring Margin (Offshore Mid-Norway): Results from Integrated Geological
1238 and Geophysical Study: Tectonics, v. 37, no. 2, p. 497-528, doi:10.1002/2017tc004655

Zastrozhnov, D., Gernigon, L., Gogin, I., Planke, S., Abdelmalak, M. M., Polteau, S., Faleide, J. I., Manton, B., and Myklebust, R., 2020, Regional structure and polyphased Cretaceous-Paleocene rift and basin development of the mid-Norwegian volcanic passive margin: Marine and Petroleum Geology, v. 115, doi:10.1016/j.marpetgeo.2020.104269

Zwingmann, H., and Mancktelow, N., 2004, Timing of Alpine fault gouges: Earth Planet. Sc. Lett., v. 223, no. 3-4, p. 415-425, doi:10.1016/j.epsl.2004.04.041

Figure 1

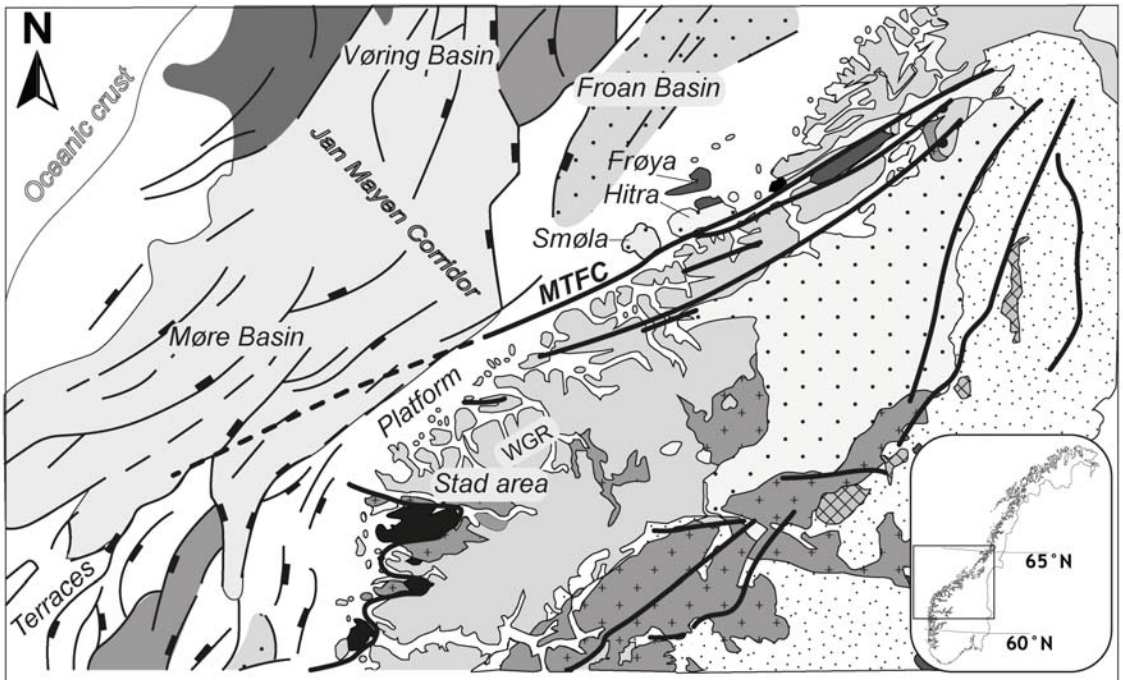

Offshore

Rift phases

- Late Cretaceous - Paleocene
- Late Jurassic - Early Cretaceous
- Late Jurassic
- Late Paleozoic

- Major normal faults
- Faults and tectonic lineaments

Onshore

Caledonian orogen

- Basin Deposits (Late Silurian - Devonian)
- Uppermost Allochthon (Neoproterozoic - Ordovician)
- Upper Allochthon (Mesoproterozoic - Silurian)
- Middle Allochthon (Mesoproterozoic - Cambrian)
- Lower Allochthon (Mesoproterozoic - Paleozoic)

Proterozoic

- Igneous and supracrustal rocks (1700 - 900 Ma)
- Igneous Belt (1800 - 1650 Ma)

- Major tectonic lineaments

Figure 2

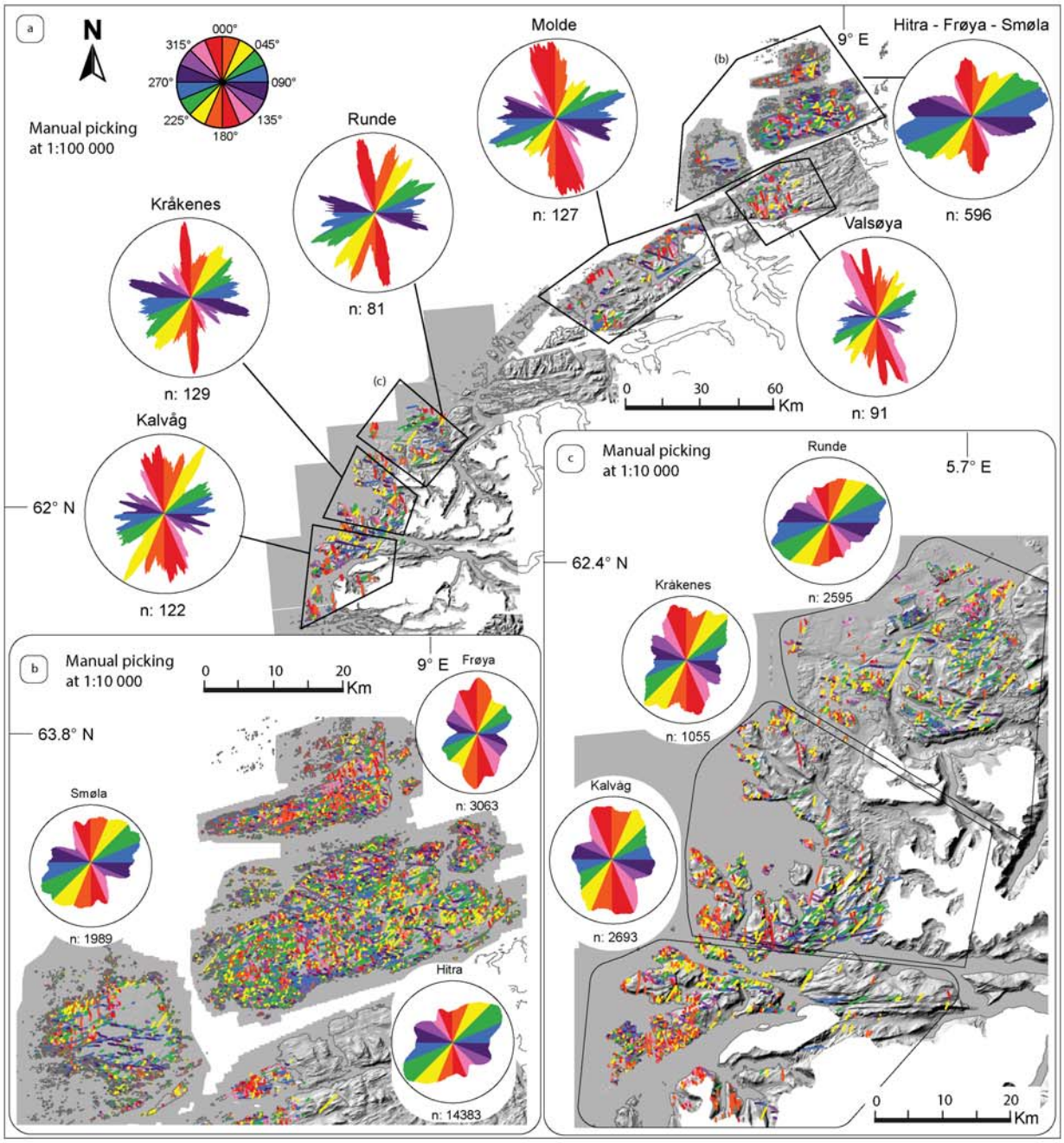
a
N
000°
045°
090°
135°
180°
225°
270°
315°
Manual picking
at 1:100 000
Molde
n: 127
Runde
n: 81
Kråkenes
n: 129
Kalvåg
n: 122
62° N
9° E
Hitra - Frøya - Smøla
n: 596
Valsøya
n: 91
(b)
(c)
0 30 60 Km
b
Manual picking
at 1:10 000
0 10 20 Km
9° E
63.8° N
Frøya
n: 3063
Smøla
n: 1989
Hitra
n: 14383
c
Manual picking
at 1:10 000
5.7° E
62.4° N
Runde
n: 2595
Kråkenes
n: 1055
Kalvåg
n: 2693
0 10 20 Km

Figure 3

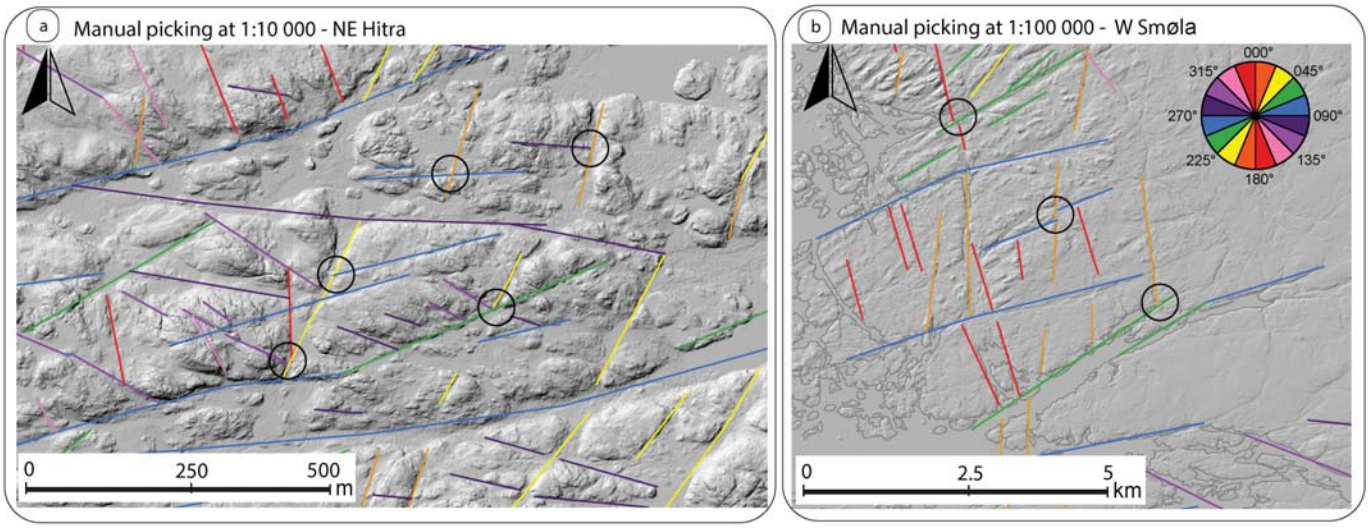
a
Manual picking at 1:10 000 - NE Hitra
0
250
500
m
b
Manual picking at 1:100 000 - W Smøla
000°
045°
090°
135°
180°
225°
270°
315°
0
2.5
5
km

Figure 4

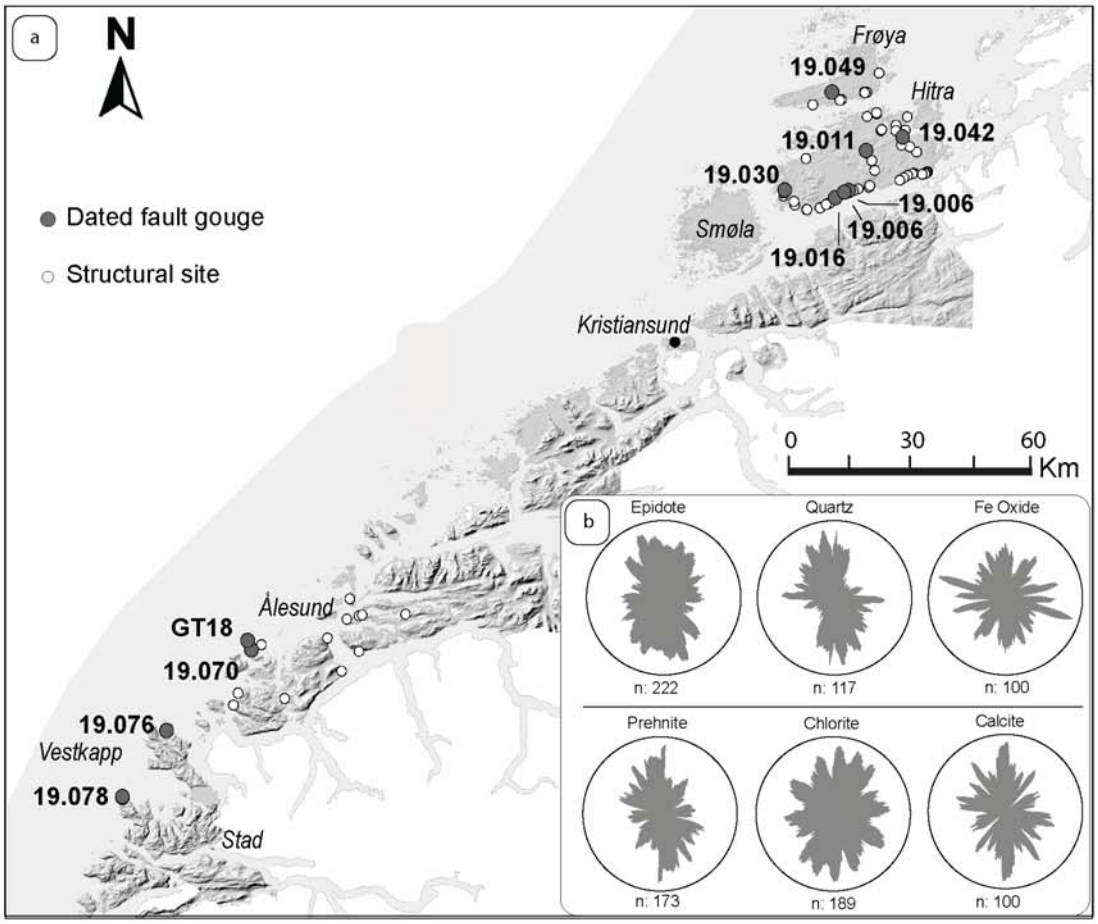
a
N
Dated fault gouge
Structural site
Frøya
19.049
Hitra
19.042
19.011
19.030
19.006
Smøla
19.006
19.016
Kristiansund
0
30
60
Km
b
Epidote
Quartz
Fe Oxide
n: 222
n: 117
n: 100
Prehnite
Chlorite
Calcite
n: 173
n: 189
n: 100
Ålesund
GT18
19.070
19.076
Vestkapp
19.078
Stad

Figure 5

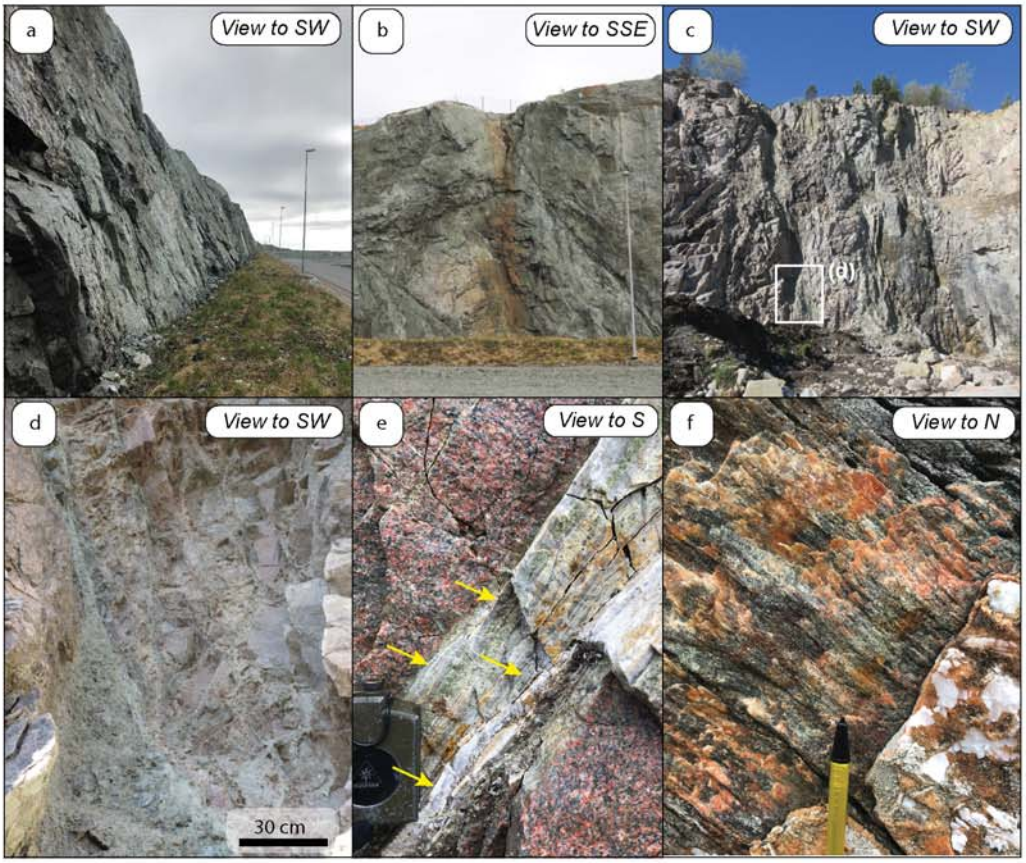
a
View to SW
b
View to SSE
c
View to SW
(d)
d
View to SW
30 cm
e
View to S
f
View to N

Figure 6


WNW - ESE - W
a
25 cm
19.006B
b
19.078
c
19.016
ENE - WSW
d
19.007A
e
19.011
f
19.042A
g
19.042E
h
GT18
i
GT18_02
GT18_01
NNE - SSW
j
19 030
19.030A
k
19.049
l
19.070
m
1 m
19.076
Key
Principal Slip Surface
Sampling area

Figure 7

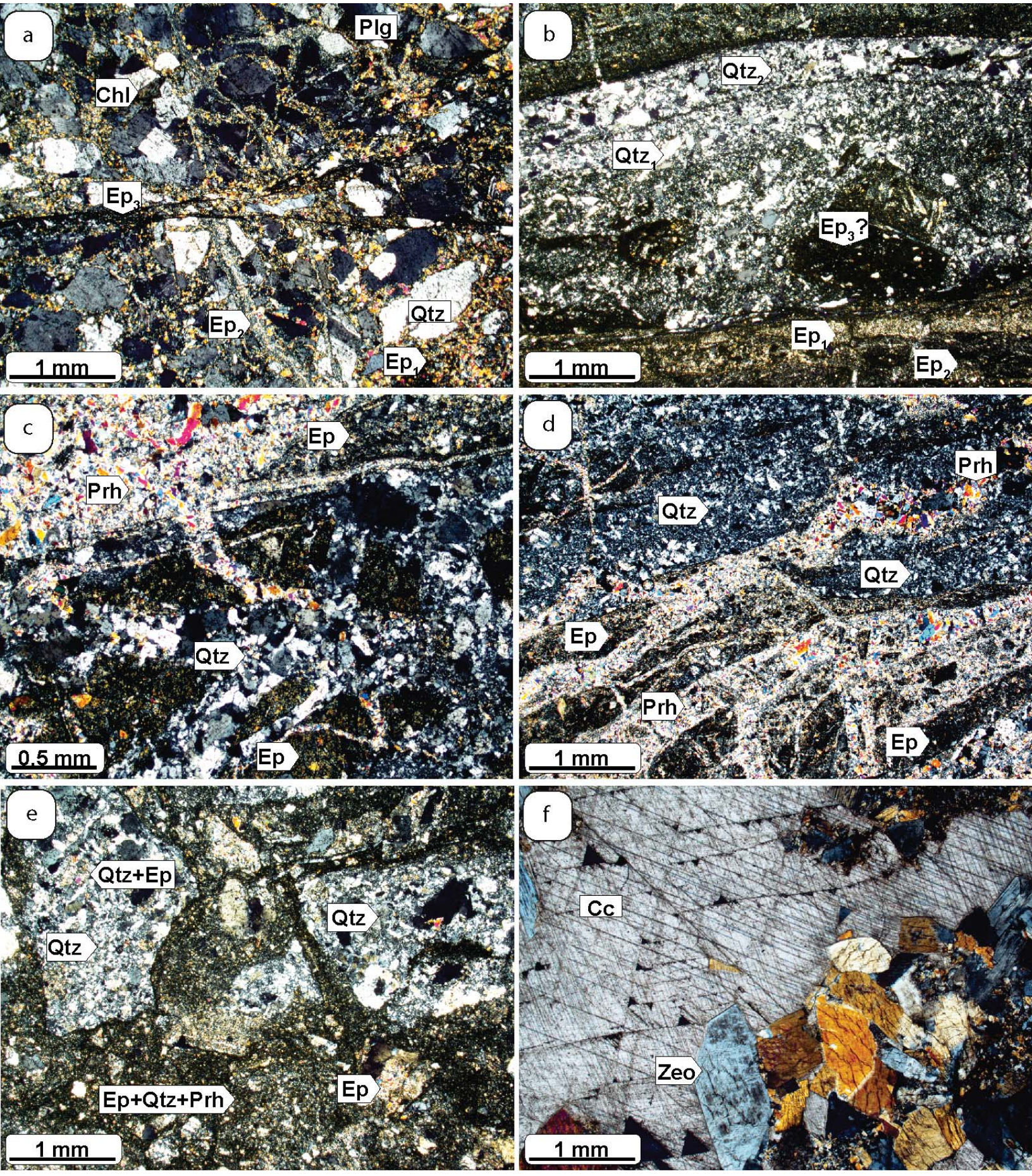
a
Plg
Chl
Ep3
Ep2
Qtz
Ep1
1 mm
b
Qtz2
Qtz1
Ep3?
Ep1
Ep2
1 mm
c
Ep
Prh
Qtz
0.5 mm
Ep
d
Prh
Qtz
Qtz
Ep
Prh
Ep
1 mm
e
Qtz+Ep
Qtz
Qtz
Ep
Ep+Qtz+Prh
1 mm
f
Cc
Zeo
1 mm

Figure 8

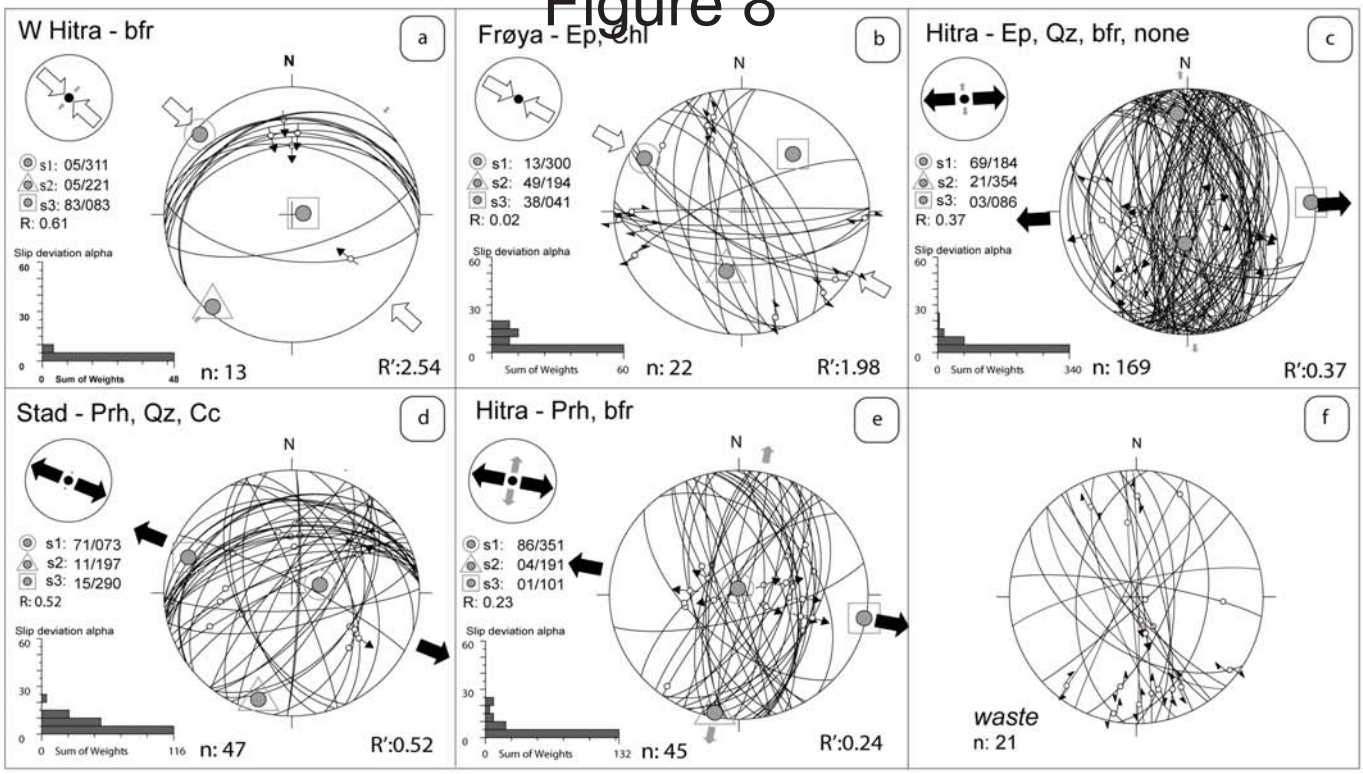
W Hitra - bfr
a
s1: 05/311
s2: 05/221
s3: 83/083
R: 0.61
Slip deviation alpha
n: 13
R':2.54
Frøya - Ep, Chl
b
s1: 13/300
s2: 49/194
s3: 38/041
R: 0.02
Slip deviation alpha
n: 22
R':1.98
Hitra - Ep, Qz, bfr, none
c
s1: 69/184
s2: 21/354
s3: 03/086
R: 0.37
Slip deviation alpha
n: 169
R':0.37
Stad - Prh, Qz, Cc
d
s1: 71/073
s2: 11/197
s3: 15/290
R: 0.52
Slip deviation alpha
n: 47
R':0.52
Hitra - Prh, bfr
e
s1: 86/351
s2: 04/191
s3: 01/101
R: 0.23
Slip deviation alpha
n: 45
R':0.24
f
waste
n: 21
N
Sum of Weights

Figure 9

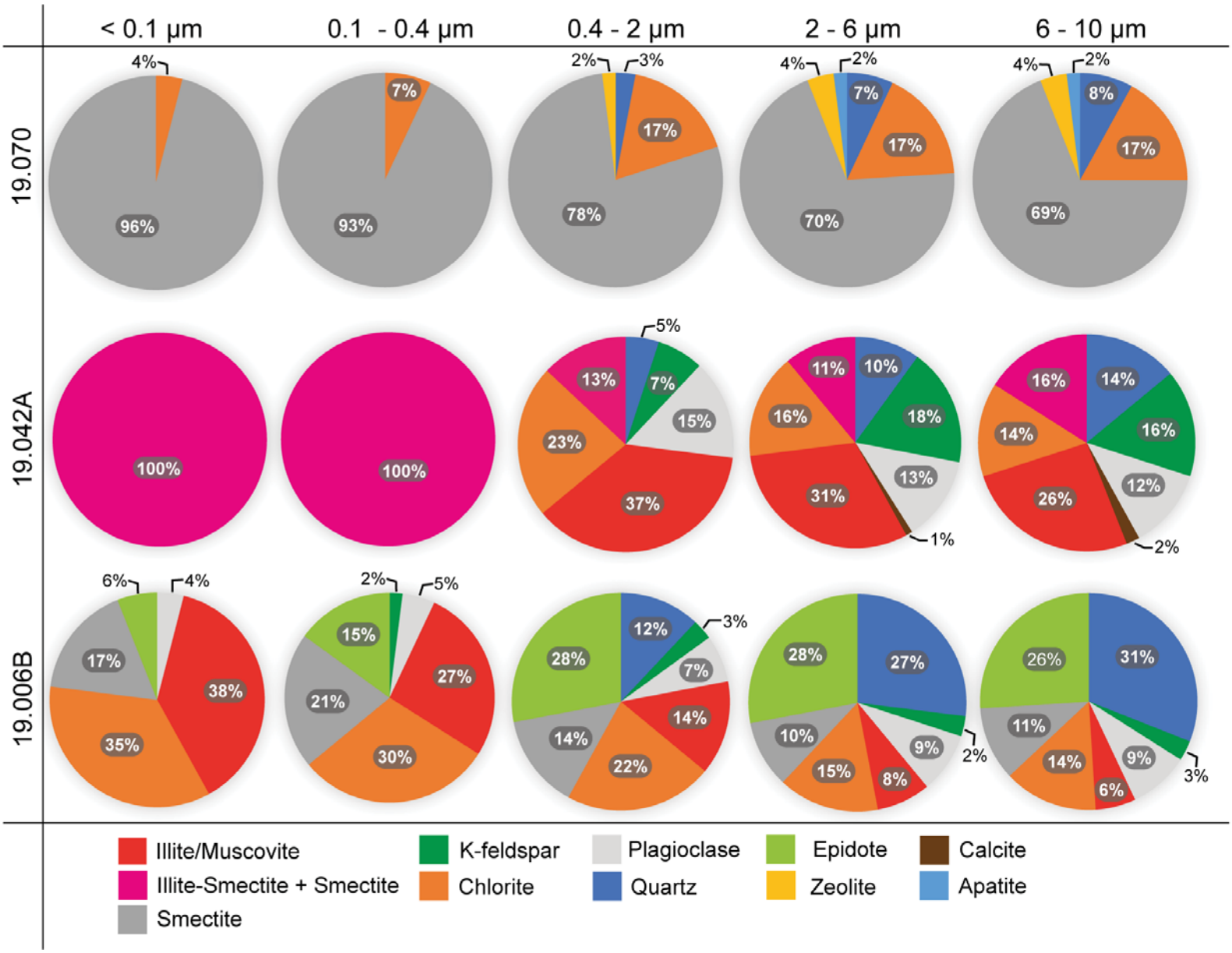
< 0.1 µm
0.1 - 0.4 µm
0.4 - 2 µm
2 - 6 µm
6 - 10 µm
19.070
19.042A
19.006B
Illite/Muscovite
Illite-Smectite + Smectite
Smectite
K-feldspar
Chlorite
Plagioclase
Quartz
Epidote
Zeolite
Calcite
Apatite

Figure 10

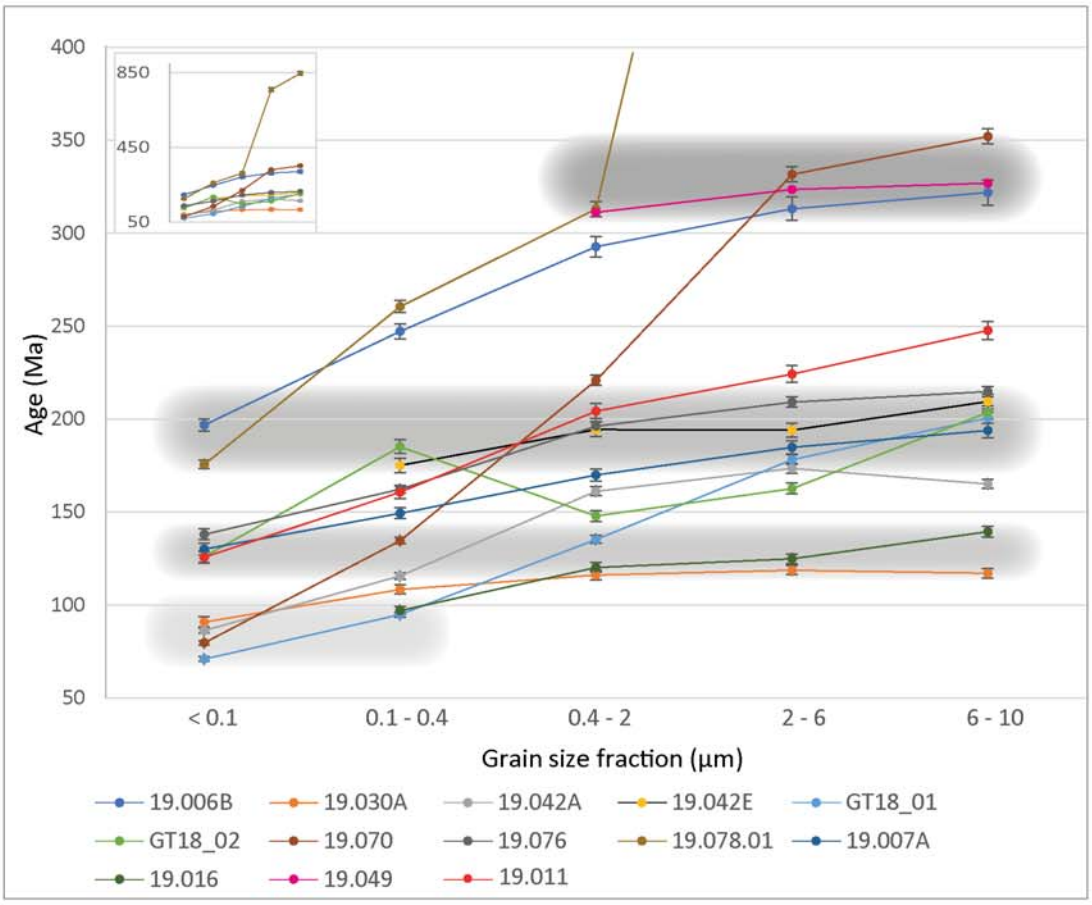
400
350
300
250
200
150
100
50
Age (Ma)
850
450
50
< 0.1
0.1 - 0.4
0.4 - 2
2 - 6
6 - 10
Grain size fraction (µm)
19.006B
19.030A
19.042A
19.042E
GT18_01
GT18_02
19.070
19.076
19.078.01
19.007A
19.016
19.049
19.011

Figure 11

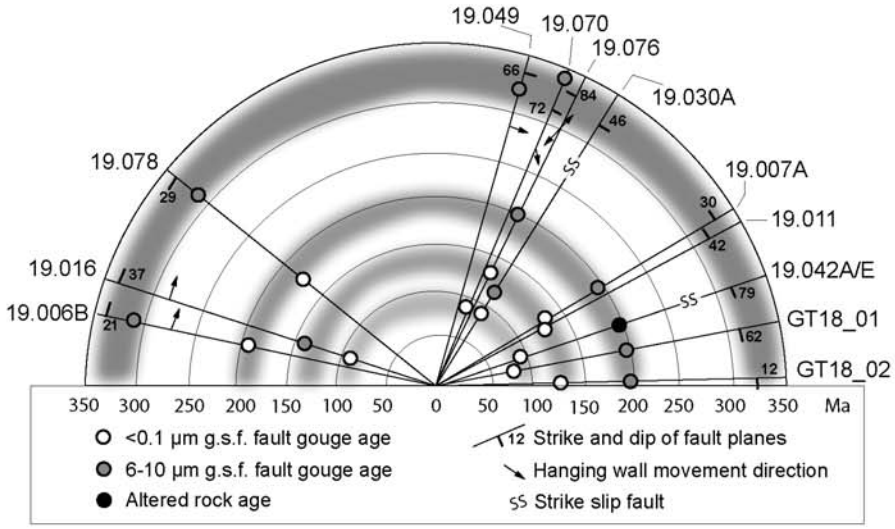
19.049
19.070
19.076
19.030A
19.007A
19.011
19.042A/E
GT18_01
GT18_02
19.078
19.016
19.006B
66
72
84
46
SS
30
42
79
62
12
29
37
21
350 300 250 200 150 100 50 0 50 100 150 200 250 300 350 Ma
<0.1 µm g.s.f. fault gouge age
6-10 µm g.s.f. fault gouge age
Altered rock age
12 Strike and dip of fault planes
Hanging wall movement direction
SS Strike slip fault

Figure 12

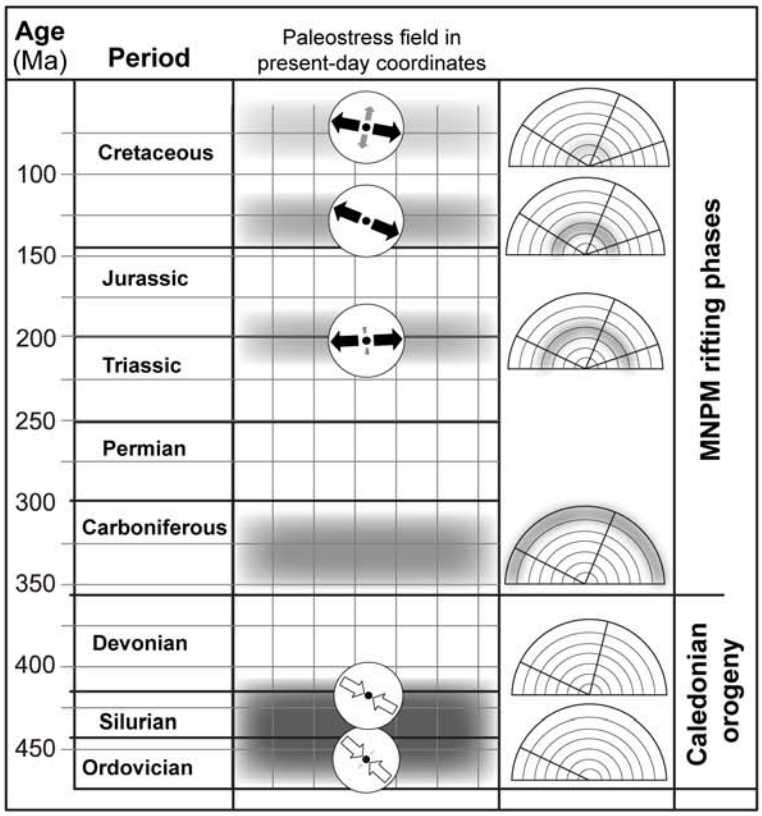
Age
(Ma)
Period
Paleostress field in
present-day coordinates
100
150
200
250
300
350
400
450
Cretaceous
Jurassic
Triassic
Permian
Carboniferous
Devonian
Silurian
Ordovician
MNPM rifting phases
Caledonian
orogeny

Table 1.

Set	Sample ID	Locality	Coordinates (WGS84)		Host Rock	Strike	Fracture Plane		Slip Line		Slip	Description of fault core	Mineralization
			N	E			Dip Dir	Dip	Trend	Plunge			
WNW-ESE and E-W	19.006B	Hitra	63°28.339'	08°40.505'	Granite	103	13	21	344	27	N	reddish and grey gouges	Subparallel calcite vein
	19.016	Hitra	63°28.116'	08°39.247'	Granodiorite	108	18	37	4	30	I/N	4-cm-thick gouge	calcite vein and zeolite
	19.078	Kråkenes	62°02.087'	04°59.667'	Gabbro	129	219	29				grey light blue gouge and reddish gouge layer	none
ENE-WSW	19.007A	Hitra	63°27.347'	08°36.213'	Granite	235	325	27				cm-thick reddish gouge	Reworked network of thin calcite veins
	19.011	Hitra	63°33.823'	08°46.071'	Amphibolite	250	340	42				foliated gouge	none
	19.042A	Hitra	63° 35.661'	08° 57.858'	Granodiorite	252	162	79	86	10	X	1.5-2 m thick fault zone with clay-rich gouge and cataclasite clasts in the lower part; altered granite in the upper part	none
	19.042E	Hitra	63° 35.661'	08° 57.858'	Granodiorite								none
	GT18_01	Runde	62° 24.318'	5° 35.563'	Amphibolitic gneiss	260	170	62				foliated gouge	none
	GT18_02	Runde	62° 24.318'	5° 35.563'	Amphibolitic gneiss	270	180	12				foliated gouge cut by a high angle second generation of gouge	none
NE-SW	19.049	Frøya	63°41.762'	08°34.944'	Migmatite	196	106	66	59	52	N	cataclasite layer and gouge	quartz vein and calcite vein
	19.070	Runde	62°23.168'	05°36.732'	Amphibolitic gneiss	203	113	72	152	63	N	Reworked shear zone; grey gouge layer embedding deformed	calcite vein cuts across the fault
	19.076	Vestkapp	62°11.487'	05°11.918'	Amphibolitic gneiss	206	296	84	12	36	S	Reworked shear zone; 10-cm-thick core with gouge, cataclasite and	hematite
	19.030A	Hitra	63°28.251'	08°20.128'	Granite	212	122	46				pinkish gouge reworking cataclastic layers, embedding chunks of	Coarse-grained calcite vein

Table 2.

Sample	Grain size fraction	Qtz	Kfs	Plg	Cc	Ep	Amp	Px	Ill/Ms	mica	Palyg	Kln	Chl	Sm	Chl-Sm	Sm and Chl-Sm	Ill-Sm and Sm	Ill-Verm	Lepid	Zeo	Stb	Ap	Anl	GOF
19.006B	<0.1			4		6			38				35	17										*1.63*
	0.1-0.4		2	5		15			27				30	21										*1.81*
	0.4-2	12	3	7		28			14				22	14										*1.68*
	2-6	27	3	9		28			8				15	10										*1.68*
	6-10	31	3	9		26			6				14	11										*1.7*
19.007A	<0.1	*too little material*																						
	0.1-0.4													>95									<5	
	0.4-2	<5		5-10					trace				<5	>60									<5	
	2-6	<5		10-15					5-10				5-10	>50									<5	
	6-10	<5		10-15					5-10				10-15	>50									<5	
19.011	<0.1	*too little material*																						
	0.1-0.4								trace				<5	>95										
	0.4-2	<5		<5					<5				5-10	>80										
	2-6	<5		5-10					5-10				5-10	>70										
	6-10	<5		5-10					5-10				5-10	>70										
19.016	<0.1	*too little material*																						
	0.1-0.4			<5									trace	>90									<5	
	0.4-2	trace		<5			trace						trace	>85									<5	
	2-6	<5		5-10			trace		trace				trace	>80									<5	
	6-10	<5		5-10			trace		trace				trace	>80									<5	
19.030A	<0.1	*too little material*																						
	0.1-0.4					<10						<10		>80										
	0.4-2			9		24						10		57										*2.94*
	2-6			25		22						10	6	37										*2.48*
	6-10	2		35		19						10	6	28										*2.43*
19.042A	<0.1																100							
	0.1-0.4																100							
	0.4-2	5	7	15					37				23				13							*2.37*
	2-6	10	18	13	1				31				16				11							*2.34*
	6-10	14	16	12	2				26				14				16							*2.23*
19.049	<0.1	*too little material*																						
	0.1-0.4	*too little material*																						
	0.4-2	3		trace?	trace				30					67										*1.38*
	2-6	5		7					35				trace	53										*2.45*
	6-10	5		7					35				trace	53										*2.46*
19.070	<0.1												4	96										*4*
	0.1-0.4												7	93										*3.21*
	0.4-2	3											17	78						2				*2.48*
	2-6	7											17	70						4		2		*2.63*
	6-10	8											17	69						4		2		*2.52*
19.077	<0.1	*too little material*																						
	0.1-0.4	7											23			70								*2.32*
	0.4-2	9		4			6	6					22			53								*1.99*
	2-6	12		5			11	7	trace				20			45								*2.07*
	6-10	12		5			12	6	trace				20			45								*2.06*
19.078	<0.1									x			x	x	x				x					
	0.1-0.4									x			x	x	x				x					
	0.4-2	trace		trace									xxxx	xxxx	xxx				xx					
	2-6	x		x									xxxx	xxxx	xxx				x					
	6-10	x		x									xxxx	xxxx	xxx				x					
GT18_01	<0.1										xxxx			xxxx										
	0.1-0.4										xxxx			xxxx										
	0.4-2	trace									xxxx	trace?		xxxx										
	2-6	x	xx								xxxx	x		xxxx										
	6-10	xx	xxx								xxx	xx		xxxx										
GT18_02	<0.1																							
	0.1-0.4			trace?										xxxx				x?			x?			
	0.4-2	x		xx										xxxx				x			xxx			
	2-6	xx		xx										xxxx				x			xxxx			
	6-10	xx		xx										xxxx				x			xxx			
Altered rock sample																								
19.042E	<0.1	*too little material*																						
	0.1-0.4	*too little material*																						
	0.4-2	x		xx					xxx				xxx	xxxx										*2.36*
	2-6	x		xx					xxx				xxx	xxxx										*2.58*
	6-10	x		xx					xxx				xxx	xxxx										*2.62*

Table 3.

		$^{40}Ar^*$				K			Age Data	
Sample Name	**Fraction**	**Mass mg**	**mol/g**	**σ (%)**	**$^{40}Ar^*$ %**	**Mass mg**	**wt %**	**σ (%)**	**Age (Ma)**	**σ (Ma)**
19.006B	<0.1	2,272	9.34E-10	0.29	75.2	50.7	2,592	1.7	196.8	±3.1
	0.1-0.4	4,796	9.06E-10	0.24	82.5	50.9	1,972	1.8	247.2	±4.1
	0.4-2	2,884	6.02E-10	0.28	86.6	50.9	1,092	2	292.7	±5.4
	2-6	2,678	3.78E-10	0.32	88.5	51	0.637	2.2	313.2	±6.4
	6-10	6,752	3.23E-10	0.24	88.9	50.7	0.528	2.3	321.9	±6.8
19.007A	<0.1	2,508	4.00E-10	0.31	26.6	6.5	1.71	2.7	130	±3.4
	0.1-0.4	1,754	3.70E-10	0.39	26.7	51.6	1.37	2	149.4	±3.0
	0.4-2	4.04	5.10E-10	0.25	39.6	50.8	1.65	2	169.9	±3.3
	2-6	2.02	5.84E-10	0.32	52.1	50.4	1.73	2	184.9	±3.6
	6-10	1.58	5.96E-10	0.37	55.4	50.5	1.68	2	193.9	±3.8
19.011	<0.1	1,854	1.52E-10	0.61	12.6	10.1	0.671	2.4	125.7	±3.0
	0.1-0.4	1,898	1.85E-10	0.53	15.4	50.7	0.635	2.1	160.7	±3.4
	0.4-2	3,556	2.80E-10	0.3	19.2	52.3	0.746	2.1	204.3	±4.1
	2-6	2.56	3.43E-10	0.32	26	51.5	0.827	2.1	224.3	±4.5
	6-10	1,778	4.05E-10	0.38	33.6	53.5	0.88	2.1	247.7	±4.9
19.016	0.1-0.4	1,662	9.50E-11	0.97	13.4	50.6	0.549	2.1	97.1	±2.2
	0.4-2	1,858	1.43E-10	0.64	19.4	52.7	0.664	2.1	120.2	±2.6
	2-6	3.3	1.58E-10	0.39	23.5	50.1	0.705	2.1	125	±2.6
	6-10	2.27	1.91E-10	0.44	27.2	50.7	0.759	2.1	139.5	±2.9
19.030A	<0.1	2.31	1.20E-10	0.72	40.2	10.5	0.739	2.9	90.9	±2.7
	0.1-0.4	3,198	1.02E-10	0.61	57	51.8	0.528	2.3	108.4	±2.5
	0.4-2	2,428	1.50E-10	0.56	66.3	51.8	0.722	2.2	116.1	±2.5
	2-6	4,718	1.72E-10	0.31	79.2	50.5	0.809	2.1	118.8	±2.5
	6-10	1.76	1.81E-10	0.66	79.5	51.2	0.865	2.1	117.1	±2.5
19.042A	<0.1	3,394	4.60E-10	0.29	12.4	51.6	3,001	1.6	86.3	±1.4
	0.1-0.4	2,472	6.26E-10	0.3	18.9	51.9	3.02	1.6	115.7	±1.8
	0.4-2	2,902	9.40E-10	0.27	37.4	50.1	3,216	1.6	161.2	±2.5
	2-6	3,028	1.10E-09	0.26	49.1	50.2	3,473	1.5	173.6	±2.6
	6-10	2,644	1.01E-09	0.27	54.5	50.8	3,373	1.5	165.1	±2.5
19.049	0.4-2	1,104	1.27E-09	0.43	86.5	25.2	2.15	2.1	311.3	±6.2
	2-6	1,646	1.36E-09	0.33	87.4	50.6	2.21	1.9	323.6	±5.9
	6-10	1,744	1.47E-09	0.32	89.8	53.9	2.37	1.9	326.9	±5.8
19.07	<0.1	3,444	1.88E-10	0.37	28.4	50.1	1.33	1.3	79.6	±1.1
	0.1-0.4	2,202	3.42E-10	0.36	43.6	52.6	1.41	1.3	134.7	±1.7
	0.4-2	2,206	7.70E-10	0.3	69.9	54.3	1.89	1.2	220.9	±2.7
	2-6	1,554	1.06E-09	0.35	83.3	51.2	1.68	1.3	331.7	±4.0
	6-10	2,058	1.15E-09	0.3	85	54	1.7	1.3	352.1	±4.1
19.076	<0.1	1,036	3.26E-10	0.68	41.5	7.1	1.31	2.2	138.1	±3.0
	0.1-0.4	2.39	3.89E-10	0.33	55.9	50.3	1.32	1.3	162.4	±2.1
	0.4-2	1,936	4.75E-10	0.36	66.2	52.4	1.32	1.3	196.2	±2.5
	2-6	2,268	4.66E-10	0.32	68.3	52.7	1.21	1.3	209.2	±2.7
	6-10	2.75	4.71E-10	0.29	71	51.7	1.19	1.3	214.8	±2.8
19.078	<0.1	0.736	6.21E-10	0.7	32.5	51.5	1.94	1.2	175.7	±2.4
	0.1-0.4	1,596	9.14E-10	0.35	37.3	50.8	1.88	1.3	260.6	±3.2
	0.4-2	1.13	7.65E-10	0.46	37.6	54.8	1.29	1.3	312.9	±4.0
	2-6	1,766	7.07E-10	0.34	38.4	51.7	0.432	1.5	759.4	±9.6
	6-10	1,456	8.56E-10	0.38	47.6	51.1	0.456	1.5	847.8	±10.5
GT18_01	<0.1	1,868	1.93E-10	0.58	20.5	50.9	1,533	1.79	71	±1.3
	0.1-0.4	3,094	3.69E-10	0.3	32.5	49.9	2,183	1.64	94.9	±1.5
	0.4-2	4,078	6.08E-10	0.26	48.3	50.3	2,493	1.58	135.3	±2.1
	2-6	2.1	9.03E-10	0.31	65.3	50.6	2.78	1.53	178.2	±2.6
	6-10	1,694	1.06E-09	0.34	74.2	49.9	2,879	1.52	200.8	±3.0
GT18_02	<0.1	2,028	1.74E-10	0.6	40.3	23.2	0.768	2.48	126	±3.1
	0.1-0.4	1,792	3.10E-10	0.45	55.2	50	0.917	2.03	185.2	±3.7
	0.4-2	1.91	2.99E-10	0.44	54.8	50.5	1.12	1.93	147.8	±2.8
	2-6	1,604	3.91E-10	0.44	65.7	49.7	1,324	1.87	162.7	±3.0
	6-10	1,592	5.07E-10	0.4	69.1	50.8	1,356	1.85	203.6	±3.6
Altered rock sample										
19.042E	0.1-0.4	1,822	2.94E-10	0.45	37.4	30.7	0.921	2.3	175.2	±3.9
	0.4-2	2.44	3.49E-10	0.34	42.7	50.2	0.98	2	194.4	±3.8
	2-6	3,112	3.96E-10	0.29	47.9	51	1,115	2	194	±3.7
	6-10	1,988	4.42E-10	0.36	53.4	50.2	1,147	2	209.5	±4.0